Engineering Structures 242 (2021) 112524

Contents lists available at ScienceDirect

Engineering Structures

journal homepage: www.elsevier.com/locate/engstruct

Modelling the experimental seismic out-of-plane two-way bending response of unreinforced periodic masonry panels using a non-linear discrete homogenized strategy

S. Sharma [a], L.C. Silva [b], F. Graziotti [c], G. Magenes [c], G. Milani [d,*]

[a] Lead Analyst, Hopper Engineering and Conultancy BV, 1072NP Amsterdam, The Netherlands (formerly Department of Civil Engineering and Architecture – DICAr, University of Pavia), Italy
[b] Lusófona University, ISISE, Faculty of Engineering, 1749-024 Lisbon, Portugal
[c] Department of Civil Engineering and Architecture - DICAr, University of Pavia and European Centre for Training and Research in Earthquake Engineering – EUCENTRE, 27100 Pavia, Italy
[d] Department of Architecture, Built Environment and Construction Engineering (A.B.C.), Technical University in Milan, 20133 Milan, Italy

ARTICLE INFO

Keywords:
Homogenization
Multi-scale
Out-of-plane
Two-way bending
Unreinforced Masonry

ABSTRACT

A non-linear discrete homogenized strategy is used to reproduce out-of-plane two-way bending shake table tests on full-scale unreinforced masonry walls. The numerical strategy represents unreinforced masonry walls as an assemblage of rigid quadrilateral plates connected through non-linear interfaces represented. The material response laws for these non-linear interfaces are derived from a homogenization procedure performed at the *meso*-scale by a finite-element plate model. This discrete model can simulate masonry orthotropy, full softening behaviour and failure. Bending and torsional deformation modes are represented. The performance of the numerical models in describing the response of the experimentally tested full-scale specimens is presented. The numerical strategy is then used to study the behaviour of unreinforced masonry walls in configurations hitherto untested. Such numerical results are then compared to state-of-the-art analytical approaches. Potential avenues of improvement for the implemented analytical methods are also highlighted.

1. Introduction

The out-of-plane (OOP) response of unreinforced masonry (URM) walls is a complex and ill-understood subject in the field of structural seismic analysis [1,2]. OOP excitation of URM walls tends to trigger two different types of response, i.e. the one-way bending and the two-way bending cases. Post-earthquake scenarios indicate OOP two-way bending to be the most common failure mode for URM walls [3-7]. This results from the fact that URM walls are generally found to be laterally supported in both horizontal and vertical edges rather than unsupported. Furthermore, one-way bending of URM wall has been extensively studied through both experimental [8-12] and numerical studies [13-16]. In converse, two-way bending has received less attention and is considered to be more complex due to masonry anisotropy, structural indeterminacy of wall configurations and internal flexural stresses acting along both directions [17]. Experimentation is still of paramount importance to thoroughly understand the behaviour of URM in OOP two-way bending. While there is some existing literature on the OOP two-way bending response of URM walls ([18-24]), recent works presented by Graziotti *et al.* [25] and Sharma *et al.* [26] addressed what was critically missing, i.e. dynamic experiments on full-scale URM panels in a two-way bending configuration. These experimental campaigns [25,26] and the data generated from them [27,28] were used as a reference in this study.

A plethora of numerical strategies can be found in the literature for the structural analysis of URM structures. Although such strategies may differ in the method and scale of analysis, it is important to note that the selection of the most appropriate method is largely dependent on the problem at hand [29]. Storey-mechanism [30,31] and equivalent-frame based approaches [32-38] preclude OOP failure modes, and were consequently unsuitable to be used in this work. In this context, it is important to mention works by Vanin *et al.* [39,40], in which the authors

* Corresponding author.
E-mail addresses: s.sharma@hopperengineers.com (S. Sharma), luis.silva@ulusofona.pt (L.C. Silva), francesco.graziotti@unipv.it (F. Graziotti), guido.magenes@unipv.it (G. Magenes), gabriele.milani@polimi.it (G. Milani).

https://doi.org/10.1016/j.engstruct.2021.112524
Received 17 December 2020; Received in revised form 24 April 2021; Accepted 9 May 2021
Available online 2 June 2021

tried to overcome the limitations of such methods. More sophisticated finite element (FE) based methods can be employed at different geometric scales. For instance, the URM components (units and mortar) are explicitly discretised at the *meso*-scale; and at the coarser macro-scale this is forfeited, being an equivalent homogeneous material assumed. Approaches at the *meso*-scale are accurate and can be used to capture the OOP response of URM. These require, however, detailed knowledge on the mechanical behaviour of the masonry components. The setback of such a level of detail is the large number of input parameters required [41] and the intense computational effort associated [42], thus limiting their application to small scale studies [43-48]. In contrast, macro-scale approaches [49-54] using continuum FE are associated with low computational effort as URM is represented by a homogenous material whose behaviour is specified by closed form laws. Yet, closed form solutions often need to be validated (or calibrated) with experimental data obtained either from in-situ or laboratory experimental investigations. Apart from FE-based numerical models, one may also address discrete/distinct element models (DEM), since these allow to represent the mechanical behaviour of masonry structures through a *meso*-modelling approach. In such models, masonry units are modelled as rigid or deformable blocks while joints are modelled as contact surfaces. DEM is especially suited for modelling the collapse of URM and other problems in case large relative displacements occur. However, when analysing the OOP behaviour of URM structures, the accuracy of DEM models is largely dependent on the number of contact points [55]. Hence, DEM models tend to require significant computational costs. In this context, special mention must be made of the applied element method (AEM) which tries to address several disadvantages associated with DEM methods and has been also applied to simulate the behaviour of URM by Mayorca and Meguro [56] and Malomo *et al.* [57].

Furthermore, homogenization based multi-scale methods have been successfully and widely used for composite materials [58,59] and represent a promising alternative. Such methods rely on a transition of information from the meso to the macro-scale and are hence designated as multi-scale or FE^2 approaches (when finite element approaches are adopted at both scales). Yet, as demonstrated in the literature, a completely continuum based FE^2 approach can lead to a high computational effort [60]. Such a shortcoming has however been circumvented by several researchers through the use of discrete FE-based models – at the macro-scale – along with other simplifications at both scales of the problem [61-66]. Such a numerical strategy can provide a good tradeoff between the advantages and disadvantages associated with other modelling techniques (read continuum FE based approaches and DEM), in terms of accuracy of the results as well as the computational effort involved. Accordingly, a non-linear discrete homogenized strategy has been used in this study. As per such a strategy, walls are modelled as an assemblage of quadrilateral rigid plates interconnected by interfaces composed by a system of non-linear deformable trusses and rigid beams. The non-linear material information required for the deformable trusses is derived by performing a homogenization step at the *meso*-scale. A two-dimensional FE based model was also used at the *meso*-scale to further reduce the overall computational effort associated with the numerical strategy.

The adopted reference experimental campaigns and numerical strategy are first presented. The validation of the numerical strategy against experimental data is then carried out along with the calibration of the input parameters. It will be noted that enough experimental data was available in the reference experimental campaigns to proceed also with a FE based *meso*-modelling strategy for the tested URM panels. However, such a choice would result in prohibitive computational effort. Consequently, a homogenization based discrete strategy was adopted keeping in mind wider future applications of the numerical strategy including (but not limited to) extensive parametric and probabilistic studies. The validated numerical strategy after calibration was then used to understand the behaviour of URM walls under OOP two-way bending action in experimentally untested configurations. State-of-the-art analytical formulations [67-71] that had been validated against the experimental results in the reference experimental campaigns [25,26] were then applied against the numerical results to further test their efficiency.

2. Reference experimental campaigns

Incremental dynamic testing of full-scale URM walls under two-way bending excitation was carried out by Graziotti *et al.* [25] and Sharma *et al.* [26]. These tests were carried out as part of a larger experimental campaign to assess the vulnerability of URM buildings under the action of induced seismicity in Groningen (the Netherlands) [72]. Four full-scale single leaf walls, with different boundary conditions, were tested in Graziotti *et al.* [25]. Three of these walls (CS-005-RR, CS-000-RF, CSW-000-RF in Table 1) were constructed in calcium silicate (CS) brick masonry and were experimentally demonstrated to be of a "Weak Unit-Strong Joint" (WU-SJ) URM typology. In this context, URM can be broadly distinguished into two distinct typologies based on their response under pure-horizontal bending. The first typology can be classified as "Weak Unit-Strong Joint" (WU-SJ) and exhibits a vertical crack passing through the brick units and head joints under pure horizontal bending. The second typology corresponds to a "Strong Unit-Weak Joint" (SU-WJ) that exhibits a stepped crack passing through head joints and half a bed joint under pure horizontal bending. It may be pointed out that: (i) specimen CS-005-RR was restrained on all four edges and subjected to a vertical pre-compression of 0.010 MPa which was reduced, during the testing sequence, to 0.005 MPa when the collapse of the specimen occurred; (ii) both CS-000-RF and CSW-000-RF walls had their top edge free and unloaded while the other three edges were restrained; (iii) the CSW-000-RF wall (Fig. 1b) was characterised by the presence of an eccentric opening ($1.79 \times 2.95 m^2$) that corresponds to almost 25% of the wall area; and (iv) Specimen CL-000-RF (Fig. 1a) was constructed in clay (CL) brick masonry and is characterized belonging to a "Strong Unit-Weak Joint" (SU-WJ) typology, being also tested with all three edges restrained and the top edge free. A cavity wall consisting of a leaf each in both CS and CL masonry connected by metal ties was also tested in [25], but has not been considered in this study.

Four single leaf CS (WU-SJ) masonry walls were tested by Sharma *et al.* [26]. If compared with the masonry walls tested by Graziotti *et al.* [25], these walls were constructed with similar brick units but weaker (intentionally) mortar. Two specimens (CS-000-RF2 and CS-000-RFV) follow the same boundary conditions of CS-000-RF [25]; which allows providing conclusive information on the behaviour of WU-SJ URM walls tested in this configuration. Of these specimens, CS-000-RFV was subjected to a simultaneous horizontal and vertical dynamic excitation. Additionally, two walls with two adjacent edges free were also tested; among which only one was tested until peak strength and collapse, i.e. CS-000-L2. Hence, only CS-000-L2 wall has been considered in this study. The walls have approximate dimensions of $4.00 \times 2.75 m^2$ (length $\times$ height), except for CS-000-L2 wall with $2.21 \times 2.75 m^2$ (length $\times$ height). Returning walls with 1 m length with perfect interlocking were constructed to guarantee the full moment transmission (i.e. restrained edges are completely fixed). A more detailed description on how the boundary conditions of the panels were realised in the laboratory, along with an analysis of the degree of restraint achieved based on the theory of vibration of plates [73], has been provided in section 4.1. The reader is referred to [25] and [26] for more details on the testing setup (Fig. 1c). A summary of the main features of the specimens can be found in Table 1.

Characterization tests were carried out for both the addressed experimental campaigns to evaluate the mechanical parameters of the used masonry, namely: Young's modulus in compression (E); strength of masonry in compression (f_m) and flexure perpendicular to bed joints (f_{mt}); strength under compression (f_c) and flexure of mortar (f_t); strength

Table 1
Tested full-scale walls considered for this study: geometries and envisaged boundary conditions.

	Specimen	l [m] h [m]	m [kg]	σ_v wall [MPa]	σ_v Retaining wall [MPa]	Horizontal restraint condition	Scheme
	CS-005-RR	3.98 2.75	2056	0.05	0.05	Fixed (R) Free (F)	
Graziotti *et al.* [25]	CS-000-RF	3.98 2.75	2056	0	0.05	Fixed (R) Free (F)	
	CSW-000-RF	3.98 2.75	1530	0	0.05	Fixed (R) Free (F)	
	CL-000-RF	4.02 2.76	2178	0	0.05	Fixed (R) Free (F)	
Sharma *et al.* [26]	CS-000-RFV	3.98 2.75	2056	0	0.05	Fixed (R) Free (F)	
	CS-000-L2	2.21 2.75	1140	0	0.05	Fixed (R) Free (F)	
	CS-000-RF2	3.98 2.75	2056	0	0.05	Fixed (R) Free (F)	

Fig. 1. (a) Specimen CL-000-RF [25] post-testing, (b) specimen CSW-000-RF [25] pre-testing and (c) general view of experimental setup adopted in Sharma *et al.* [26].

under compression (f_u) and flexure of units (f_{ut}); and the cohesion and friction coefficient of masonry bed joints (f_{v0} and μ) under direct shear [74-78]. The used CS and CL units measured 212x102x71mm^3 and 208x98x50 mm^3 respectively and mortar joints were always 10 mm thick. These parameters are summarized in Table 2.

All the specimens were subjected to random excitations with low amplitude (encompassing a broad frequency spectrum) before the commencement of any testing. This was done to identify the period associated with the first natural mode of vibration of the walls (Table 3). This information was used for the calibration of the numerical models.

Table 2
Mechanical properties of the masonry for the tested full-scale walls.

				E	f_m	f_{mt}	f_c	f_t	f_u	f_{ut}	f_{v0}	μ
Graziotti *et al.* [25]	**WU-SJ**	***Mean***	[MPa]	4784	9.74	0.95	8.49	2.72	15.31	2.61	0.81	0.46
	(CS)	***C.o.V.***	[%]	18.0	7.8	18.2	32.9	31.3	6.1	14.5	–	–
	SU-WJ	***Mean***	[MPa]	7497	17.41	0.41	4.51	1.15	46.80	7.83	0.18	0.63
	(CL)	***C.o.V.***	[%]	26.3	8.5	55.3	12.5	15.8	10.9	4.7	–	–
Sharma *et al.*	**WU-SJ**	***Mean***	[MPa]	5943	7.29	0.22	1.39	0.31	15.31	2.61	0.13	0.55
	(CS)	***C.o.V.***	[%]	9.6	11.75	51.1	31.9	50.3	6.1	14.5	–	–

Table 3
Period associated with the first natural (fundamental) mode of vibration of the walls (measured experimentally).

Graziotti *et al.* [25]			Sharma *et al.* [26]		
Specimen	Frequency, f [Hz]	*Period, T* [s]	Specimen	Frequency, f [Hz]	*Period, T* [s]
CS-005-RR	22.9	0.044	CS-000-RFV	12.4	0.080
CS-000-RF	13.7	0.073	CS-000-L2	10.1	0.099
CSW-000-RF	13.5	0.074	CS-000-RF2	12.8	0.078
CL-000-RF	12.8	0.078			

3. Numerical strategy adopted

The multi-scale FE computational homogenization procedure implemented in this study comprises several steps that are described next. It is important to establish, before delving into a detailed description, the scales being referred throughout the article. In the context of this work, meso refers to a scale in which URM is discretised explicitly into its components, i.e. units and mortar. In contrast, the coarser scale is designated as macro and it represents the structural level, referring to the space that a structure is discretized explicitly only into its geometric features. While a complete description of the theoretical considerations involved in the homogenization process lies outside the scope of this paper, an interested reader is referred to Silva *et al.* [79,80]. Here, this section intends only to provide a general description of the application of the three steps involved in the adopted numerical strategy while carrying out the current work.

3.1. Meso-scale: Modelling the representative volume element

The first step is performed at the *meso*-scale and consists of the definition of a representative volume element (RVE). Considering the periodic nature of the masonry texture being analysed, the definition of the RVE was done following the recommendations of Anthoine [81]. This repeating volume unit is given in Fig. 2b and consists of a full masonry unit flanked by halved (1/2) head joints on both sides. Two full bed joints are present on both the top and bottom of this central layer. These bed joints are topped by two quarters (1/4) of units which are separated by a complete head joint. It is important to note that other RVE's could be also defined, as long as when assembled the periodic masonry pattern can be reproduced.

The adopted numerical approach allows the use of different modelling strategies at the *meso*-scale to model the RVE. Three-dimensional continuum models within detailed *meso*-modelling approaches that include the explicit representation of units, mortar joints and unit-mortar interface are known to provide accurate results. Still, this level of accuracy comes with a prohibitive computational cost and it can be challenging to find a good and stable solution within highly non-linear problems [82,83]. Moreover, it has already been mentioned that one of the goals of the current study is to develop and validate a fast and computationally attractive strategy capable of simulating the OOP two-way bending behaviour of URM. A Kirchhoff-Love plate model [79] was adopted based on such reasoning.

Masonry units of the RVE were modelled as linear elastic quadrilateral FE plate elements with a linear interpolation scheme (Fig. 3e). As already mentioned in section 2, the CL brick masonry of specimen CL-000-RF corresponded to a SU-WJ typology, while CS masonry of all other specimens corresponded to a WU-SJ typology. The FE model of the RVE had to take this into account and, therefore, an interface element was provided at the units mid-length for the WU-SJ masonry case (Fig. 3b). This mid-length interface was not present in the RVE of the SU-WJ case (Fig. 3a). It is interesting to note here that brick units (continuous media) could be described by a nonlinear material behaviour. Such assumption would offer a more realistic mechanical description of the masonry, especially in the presence of significant compression stress levels that could lead to the crushing of units, as seen in [1,2]. The assumption of predefining the location of cracks has been mainly supported by the considered experimental data. In particular, it has been observed that failure of bricks – for the case of WU-SJ masonry specimens – occured through vertical mid-length cracking. Other literature studies have also adopted the same modelling assumption, for instance [3-5]. Note that this is particularly recommended in the cases that brick failure is mainly governed by bending, as addressed in [5]. Furthermore, lumping the material nonlinearity of brick units within pre-defined interface elements brings advantages from a computational standpoint, i.e. the overall computational effort is lower.

Mortar joints (head and bed) in both RVE's were modelled as line interface elements with zero thickness (Fig. 3d). All material non-linearity was concentrated in these interface elements and a multi-surface plasticity model, developed by Lourenço and Rots [84], was used to describe its failure envelope. Such an interface model can reproduce crushing, frictional slip and fracture. The elastic domain is bounded by a composite yield surface that accounts for failure as well as softening in tension, shear and compression (Fig. 3c). For the WU-SJ RVE, the same so-called multisurface plasticity model [84] was also used to simulate the non-linear behaviour of the units. An exponential softening has been assumed for tension and shear modes. Under a compression mode, both hardening and softening have been assumed. The hardening onset is given for a stress three times lower than the compressive strength and the softening branch is defined by a parabolic law. For all the modes, softening is controlled by fracture energy terms,

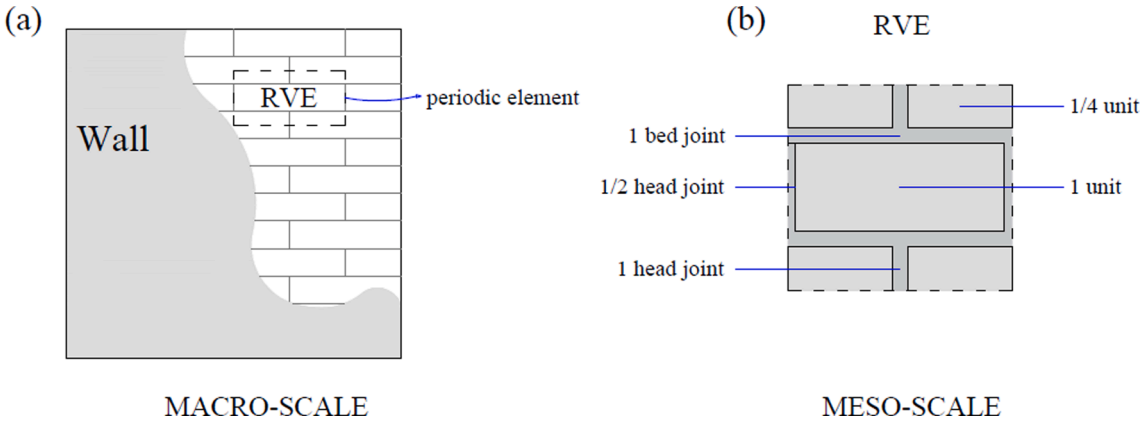

Fig. 2. Schematic representation of the periodic volume element: (a) at the macro-scale or structural level; and (b) at the *meso*-scale, in which the homogenization procedures are performed.

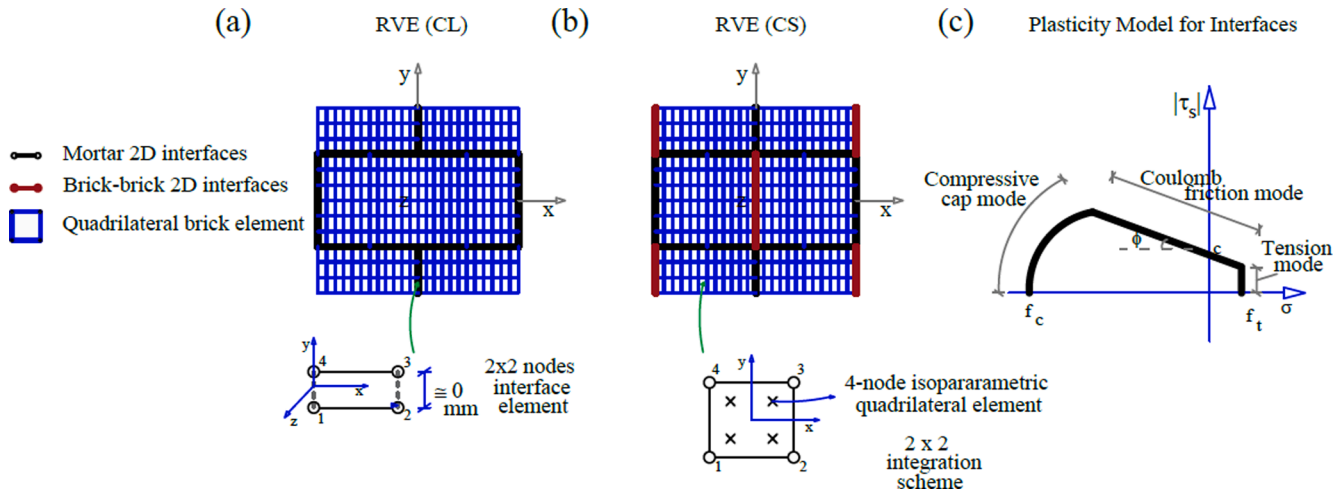

Fig. 3. Detailed description of the considered RVE FE models: (a) for the SU-WJ (clay) masonry case; (b) for the WU-SJ (CS) masonry case; and (c) plasticity model used for the interfaces.

which are reported in Table 5 ($G_f^{I,t}$ in tension, G_f^{II} in shear and $G_f^{I,c}$ in compression, respectively). A refined quadrilateral mesh with an approximate size of 8 mm was adopted for both the RVE models. However, it is important to note that several studies [85,86] point out that coarser meshes, leading to a lower computational burden, would also be adequate for this purpose.

The *meso*-scale RVE was modelled using the advanced finite element software DIANA [87]. DIANA has a vast in-built element library and well-validated advanced numerical features; for instance, an arc-length algorithm within a secant BFGS method [88] was used in this study. With the adopted numerical strategy, the RVE can account for vertical debonding at the bed joints, torsional shear failure of the bed joints (important in case of SU-WJ typology) as well as the splitting of masonry units (important in case of WU-SJ typology); in summary all modes of failure that were observed during the reference experimental campaigns.

3.2. Meso to macro scale: Homogenization

Homogenization is a procedure that is performed at the *meso*-scale and involves solving a boundary value problem (BVP) on the RVE. The solution of the BVP provides an averaged response that may be then used to describe the constitutive relations at the macro-scale. A homogenized model based on the Kirchhoff-Love plate theory was used due to its straightforward nature. A Mindlin-Reissner plate theory based model could be also adopted, as both homogenized models have been validated with very good agreement against experimental results in Silva *et al.* [79]. A brief description of the main features of the model (i.e. Kirchhoff-Love) adopted here is provided next. For a better insight on the derivation of the BVP as well as the Kirchhoff-Love homogenized model, the reader is referred to [79].

The Kirchhoff-Love plate theory based homogenized model stands on the assumption that at the *meso*-scale (scale of the RVE), URM behaviour is similar to that of a Kirchhoff-Love plate, meaning that: (i) the thickness of the plate does not change under deformation; and (ii) that straight lines normal to the mid-surface remain straight and normal to mid-surface after deformation [89]. The OOP direct stress component is also assumed to be negligible, similarly to a plane stress condition. Thus, the Kirchhoff-Love plate theory based homogenized model decouples membrane and bending behaviour, with membrane and bending behaviour being considered by a plane stress model and Kirchhoff-Love plate model respectively. The displacement vector on any point of the Kirchhoff-Love plate is denoted by $u = \left[u_x, \quad u_y, \quad u_z\right]^T$ and θ_x and θ_y denote the rotation about the global axes. The normal strains ε_z are negligible and can be ignored. The unknown strain vector can be calculated as $\varepsilon = \left[\frac{\partial u_x}{\partial x}, \ \frac{\partial u_y}{\partial y}, \ \frac{\partial u_x}{\partial y} + \frac{\partial u_y}{\partial x}, \ \frac{\partial \theta_y}{\partial x}, \ \frac{\partial \theta_x}{\partial y}, \ \frac{\partial \theta_y}{\partial y} - \frac{\partial \theta_x}{\partial x}\right]^T$. The first three terms of the strain vector denote the in-plane strains while the latter three terms denote the curvature (κ) of the mid-plane of the plate. Furthermore, it may be remarked that while the OOP shear strains (γ_{xz} and γ_{yz}) are neglected, the OOP shear forces are still indirectly considered as these are necessary to fulfil the equilibrium condition of the problem. With these assumptions in place and assuming periodic boundary conditions [85,90,91], the RVE is subjected to three modes of deformation (Fig. 4). These three modes of deformation are tension along XX (Mode I-XX), tension along YY (Mode I-YY) and shear along XY (Mode II-XY). The internal static equilibrium of the RVE is solved to obtain the mesoscopic stress (σ_m) and strain (ε_m) fields (including the κ components) respectively.

Macro-stress couples are obtained by the application of periodic fluctuations of rotations writen by curvature increments ($\Delta\chi_{11}$, $\Delta\chi_{22}$, $\Delta\chi_{12}$). A displacement driven approach has been adopted to define such macroscopic curvature increments and, therefore, suitable periodic boundary displacements are applied following the modes depicted in Fig. 4. In this context, the thickness of the masonry panel is divided into several n fibers (assumed here to be $n = 60$) and each fiber undergoes in-plane displacements within a plane-stress assumption, whose response is given via FE homogenization. Therefore, once the cross-section equilibrium is established through an iterative procedure, the moment–curvature (M-χ) quantities can be computed by the summation of the contribution of each fiber. The resultant macro-stress couples (M-χ curves) can thus be computed by the integration of the obtained mesoscopic stress along the mid-plane reference surface of the RVE, as per equation (1) (Kirchhoff-Love plate theory). It is to be noted that $M_{xy} = M_{yx}$, which is implicit from the definition of the RVE used.

$$M_{xx} = \int_{-\frac{\xi}{2}}^{\frac{\xi}{2}} \sigma_{m,xx} z dz \ (\text{Mode I} - \text{XX}) \tag{1}$$

$$M_{yy} = \int_{-\frac{\xi}{2}}^{\frac{\xi}{2}} \sigma_{m,yy} z dz \ (\text{Mode I} - \text{YY})$$

$$M_{xy} = \int_{-\frac{\xi}{2}}^{\frac{\xi}{2}} \sigma_{m,xy} z dz \ (\text{Mode II} - \text{XY})$$

3.3. Macro-scale: modelling the full-scale walls

This step includes the modelling of the walls at a macro-scale. The

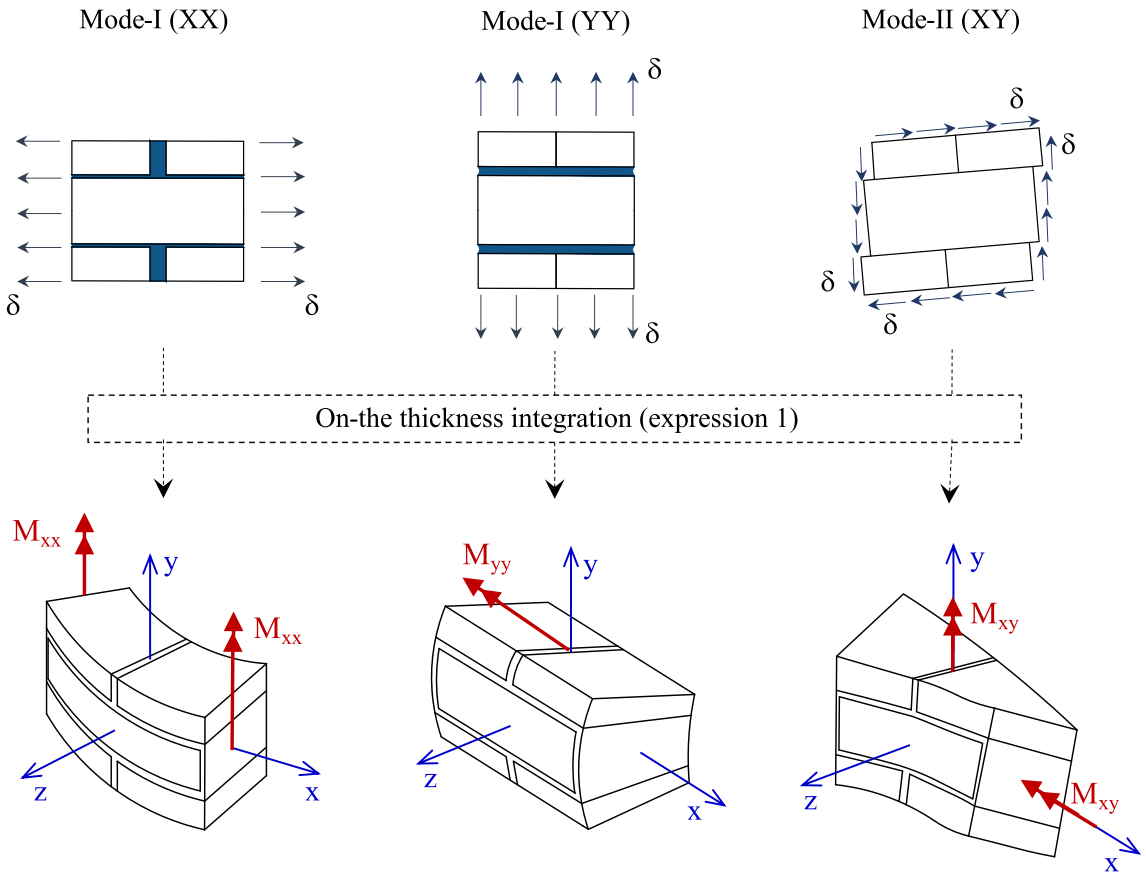

Fig. 4. Deformation modes considered together with the associated output in terms of *M*- κ curves: mode-I (XX), tension along XX; mode-I (YY), tension along YY; and mode-II (XY), shear along XY.

information from the previous step (*M*- κ curves) is considered as input for the macro-constitutive law. A discrete FE model based on the theoretical background of Rigid-Body-Spring-Mass models by Kawai [92] was used. The discrete model consists of quadrilateral rigid plates (with a nominal thickness of 10 mm) whose interfaces are provided by a set of deformable trusses and rigid beams (Fig. 5). Four different types of deformable trusses were used, in which each type accounts for a different mode of deformation of the macroscopic unit cell and, consequently, of the wall (see Fig. 6). Two of these trusses reproduce bending, i.e. vertical and horizontal bending (see Fig. 6a,b), while the others

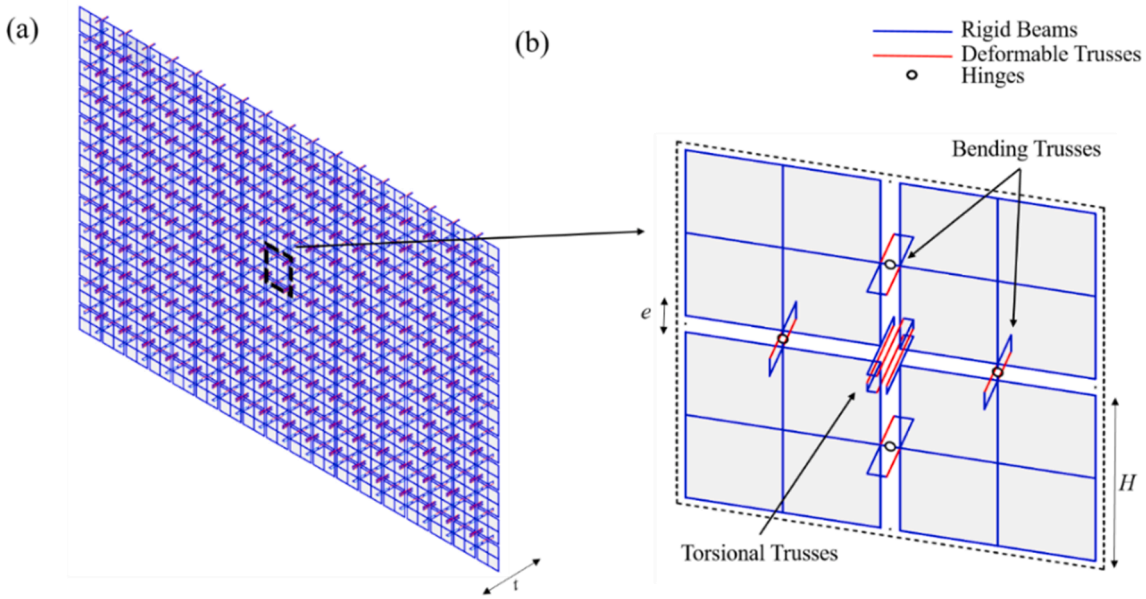

Fig. 5. Assumed discrete model at a macro-scale: (a) representation of a masonry wall; and (b) its macroscopic repeating unit.

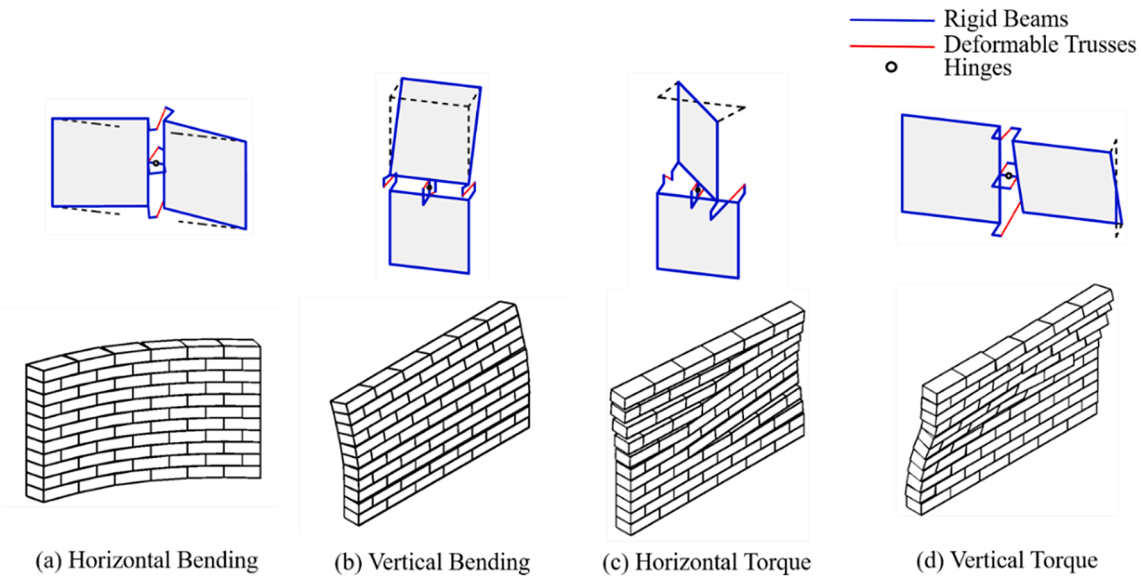

Fig. 6. Deformation modes considered for the walls: (a) horizontal bending; (b) vertical bending; (c) horizontal torque; and (d) vertical torque.

reproduce torsional deformations (see Fig. 6c,d). Bending trusses are placed at the mid-centre of the interfaces and torsional trusses are placed at its corners (Fig. 5b). Mid-span hinges are added to allow torsional movements without affecting the deformed shape (see Fig. 5b). Deformation and damage of the system are restricted only to the deformable trusses; that are analogous to springs in a Rigid-Body-Spring-Mass model since these possess a single degree of freedom. The mass of the system is assumed to be distributed on the rigid quadrilateral plates.

The discrete model was implemented in the commercially available finite element environment ABAQUS [93]. The concrete damage plasticity (CDP) model [94,95] was chosen as the constitutive material law for the deformable trusses. The CDP model can reproduce the information from the *meso*-scale at a macro-scale, in which both elastic and inelastic responses of the RVE are included. The CDP model combines a stress-based plasticity model coupled with a strain-based scalar damage model. The stress–strain relationship is, therefore, controlled by an isotropic damage scalar d as per equation (2):

$$\boldsymbol{\sigma} = (1-d)E_o(\boldsymbol{\varepsilon} - \boldsymbol{\varepsilon}^{pl}) \tag{2}$$

in which $\boldsymbol{\sigma}$ represents the nominal stress tensor, E_o the Young's modulus of the material, $\boldsymbol{\varepsilon}$ the total strain tensor and $\boldsymbol{\varepsilon}^{pl}$ the plastic strain tensor respectively. The damage parameter d can take a value between zero (undamaged material) and one (completely damaged material). The CDP model input in ABAQUS is given in terms of failure stress and strain (σ_o and ε_o in Fig. 7). To introduce the material non-linearity, post-failure values of stress and inelastic strains ($\boldsymbol{\varepsilon}^{ck}$) need to be introduced, together with the corresponding damage parameters d. In this context, $\boldsymbol{\varepsilon}^{ck}$ at any point on the σ- ε curve can be calculated as $\boldsymbol{\varepsilon}^{ck} = \boldsymbol{\varepsilon}$- $\boldsymbol{\varepsilon}_o$. The damage scalar d at any point of the σ- ε curve is calculated by associating the damaged elastic modulus of the material (E_d) with the undamaged initial elastic stiffness (E_o) as $E = E_o\ (1\text{-}d)$. An identical behaviour was assumed for the deformable trusses in compression and tension aiming to reproduce the correct forces binary of the associated OOP response. For more details on the application of the CDP model in ABAQUS the reader is referred to [96].

Thus, the M- κ curves obtained from the previous step need to be converted into σ- ε curves to serve as input for the constitutive laws for the deformable trusses. The representative stress values for the bending (σ_{BT}) and torsional trusses (σ_{TT}) were calculated through equation (3):

$$\sigma_{BT} = \frac{M}{(e.A_{BT})}; \sigma_{TT} = \frac{M}{(H.A_{TT})} \tag{3}$$

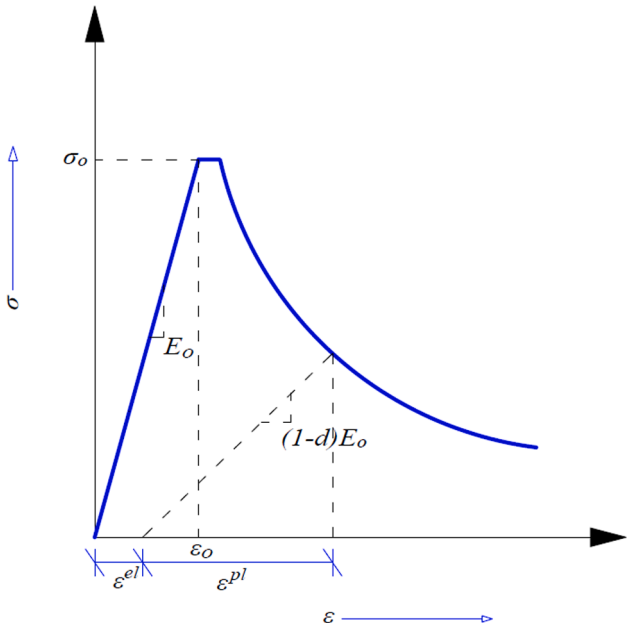

Fig. 7. Parameters associated with the Concrete Damage Plasticity model.

In equation (3), M is the bending moment per unit of interface length, e is the gap between the rigid plates, which should ideally be zero but in practice is assumed small enough to be able to place trusses between elements, while H is the length of each quadrilateral rigid plate (Fig. 5). A_{BT} and A_{TT} represent the cross-sectional area of bending and torque trusses calculated as $eH/2$. The ε values are calculated via a regularization process, which is necessary to guarantee the objectivity of the σ-ε curves from the mesh adopted at the macro-scale (especially important in the non-linear/softening range). Regularization factors are calculated as the ratio of the strain energies associated with a continuum plate model ($\prod_{continuum}$) and an equivalent discrete model ($\prod_{discrete}$) for the same deformation mode; hence ensuring a strain energy equivalence between the two models. The strain energies associated with a continuum plate under a unitary bending and torsional moment are given as:

$$\prod_{continuum,XX}^{bending} = \frac{E_{xx}Ht^3}{24(1-\nu^2)}(H+e)\left(\frac{\partial^2 u_z}{\partial x^2}\right)^2$$

$$\prod_{continuum,YY}^{bending} = \frac{E_{yy}Ht^3}{24(1-\nu^2)}(H+e)\left(\frac{\partial^2 u_z}{\partial y^2}\right)^2$$

$$\prod_{continuum,XY}^{torsion} = \frac{G_{xy}Ht^3}{24}(H+e)\left(\frac{\partial^2 u_z}{\partial x \partial y}\right)^2 \quad (4)$$

in which ν is the Poisson's ratio ($\nu = 0.2$), t is the thickness of the wall. Note that E_{xx}, E_{yy} and G_{xy} represent the homogenized elastic modulus computed at a *meso*-scale (RVE level) for mode I-XX, mode I-YY and mode II-XY deformations, respectively (Fig. 4). Similarly, the strain energy of the discrete model ($\prod_{discrete}$) associated with the two bending and torsional deformation modes are given as:

$$\prod_{discrete,XX}^{bending} = \frac{1}{2}\frac{E_{hb}A_{BT}e^2}{t/2}(H+e)^2\left(\frac{\partial^2 u_z}{\partial x^2}\right)^2$$

$$\prod_{discrete,YY}^{bending} = \frac{1}{2}\frac{E_{vb}A_{BT}e^2}{t/2}(H+e)^2\left(\frac{\partial^2 u_z}{\partial y^2}\right)^2$$

$$\prod_{discrete,XY}^{torsion} = \frac{1}{16}\frac{E_{tor}A_{TT}eH^3}{t}(H+e)^2\left(\frac{\partial^2 u_z}{\partial x \partial y}\right)^2 \quad (5)$$

In equation (5), E_{hb}, E_{vb} and E_{tor} refer to the Young's modulus of the trusses of the discrete model taking into account horizontal bending, vertical bending and torsional deformation modes respectively (Fig. 6). A_{BT} and A_T refer to the cross-sectional area of bending and torsional beams and trusses respectively. By assuring the energy equivalence between the continuum and discrete media i.e. equating the expressions from Equations (4) with their respective counterparts from Equation (5); E_{hb}, E_{vb} and E_{tor} are calculated as:

$$E_{hb} = \frac{E_{xx}t^4H}{12(1-\nu^2)(H+e)e^3H}\text{(Horizontal Bending)}$$

$$E_{vb} = \frac{E_{yy}t^4H}{12(1-\nu^2)(H+e)e^3H}\text{(Vertical Bending)}$$

$$E_{tor} = \frac{2G_{xy}t^4}{3H^2e(H+e)}\text{(Torsional moment)} \quad (6)$$

In this context, individual regularization factors can be calculated for each deformable truss. It is to be noted here that M_{xy} was assumed to be equal to M_{yx}. Consequently, though accounting for different modes of deformation of the wall (Fig. 6), the mechanical behaviour of both horizontal and vertical torsional truss is the same. Therefore, their Young's modulus is alike and are both computed from G_{xy}. It should also be noted that the Young's modulus of every deformable truss, obtained through energy equivalence, is calculated at a point (ε_p, σ_p,) in which one-third of the peak stress ($3\sigma_p$) is attained. For example, the regularization factor for the horizontal bending trusses ($f_{r,hb}$) can be calculated as per Equation (7):

$$f_{r,hb} = \frac{\sigma_p}{\varepsilon_p E_{hb}} \quad (7)$$

The obtained regularization factors are used to affect the curvature (κ) values of each curve aiming to scale and regularize them. Regularizing the strain/curvature rather than the stress/moment quantities has the additional advantage of regularizing the post-peak values and as a result the fracture energy itself. The σ- ε curves obtained by the methodology outlined in this section act as input for the CDP constitutive law assigned to the deformable truss of the discrete macro-scale model. Fig. 8 addresses the scheme that describes the steps required to gather the representative input for the CDP model at the macro (structural) scale.

4. Validation of the numerical strategy

Incremental dynamic shake table tests performed on URM walls and given in [25,26] are taken as case studies to validate the numerical strategy. Dynamic loading is fundamentally different from a static loading. The former involves subjecting the wall to a series of accelerations, while the latter involves applying a pre-defined and time-invariant load. Although in a real earthquake scenario a wall is always subjected to dynamic actions, such type of analyses leads to less control from a structural analysis standpoint and are far more computationally expensive when compared to a pushover analysis. In fact, pushover analyses allow a better characterisation of load–displacement behaviour as well as the progression of damage/cracks. For a more detailed discussion on the different behaviour exhibited by URM structures under dynamic and static loading, the reader is referred to Calvi *et al.* [97] and Graziotti *et al.* [72].

In such a context, non-linear static (pushover) analyses were performed on the studied walls (Table 1). Loading was applied on the rigid plates as a monotonically increasing uniform pressure load in the OOP direction. Implementation of the macro-scale problem in ABAQUS [93] also allowed the use of its advanced equation solving strategies such as a modified form of the Riks (viz. arc-length) method [88,98,99] and the line search algorithm, helping to overcome potential convergence problems in the highly non-linear range. Performing dynamic analyses on models of walls developed adopting the approach outlined in this article remains an avenue that needs to be explored further.

4.1. Boundary conditions

Boundary conditions can have a significant influence on the OOP response of URM panels [100,101]. In the laboratory, the restraint along the vertical edges of the tested walls was achieved with return walls of 1 m length and full interlocking: alternating rows of headers from the wall and stretchers from the return walls. The return walls were pre-

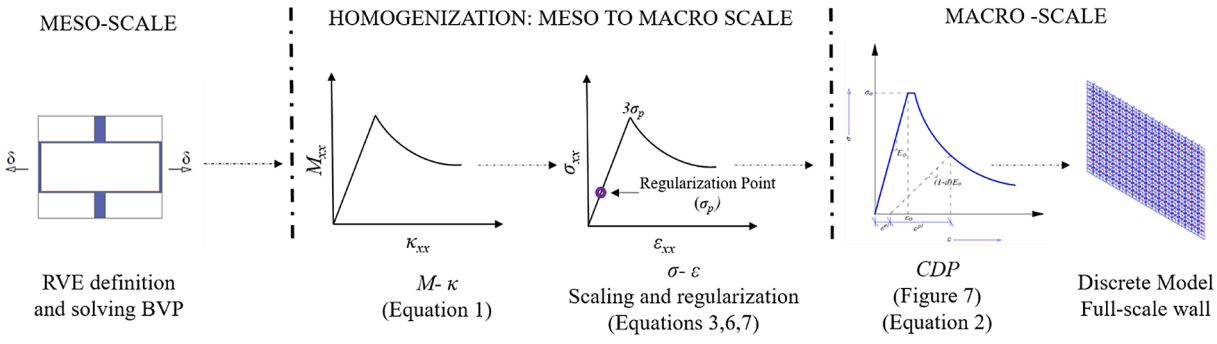

Fig. 8. Scheme outlining the transferring of the material information between scales (the represented curves are hypothetical).

compressed with an overburden of 0.05 MPa and were effectively restrained from any OOP movement. Restraint along the bottom edge was in the form of a mortar joint between the lowermost course of bricks and a RC foundation anchored to the shake table. In the case of CS-005-RR wall, restraint at the top edge was provided by steel profiles clamping the top layer of bricks and by using high strength mortar to fill the gap between the bricks and the profiles. Considering the different methods adopted, it is unlikely that vertical and bottom edges provide the same degree of restraint. This is also supported by the crack pattern/failure mechanism observed experimentally for CS-005-RR in [25].

In fact, it has already been reported in Sharma *et al.* [26], through the theory of plates, that the experimentally measured displacement at the peak load capacity corresponded to a degree of restraint that lies in between a fully fixed and simply support for the vertical edges. For the sake of simplicity and since different construction methods were used at the vertical and horizontal edges, an intermediate fixity (between fixed and simply supported) was adopted only at the vertical edges and full moment transmission (fixed boundary condition) was assumed for the restrained horizontal edges. Such an assumption is also justified by experimental observations, in which horizontal cracks controlled by the vertical bending response (and the degree of fixity at horizontal edges) of masonry typically occur before the peak load capacity of wall is reached and are therefore unlikely to contribute to their full capacity [102-104]. An intermediate support condition i.e. between a fully fixed and simply supported scenario was simulated by providing another set of rigid and linear-elastic deformable trusses at the vertical edges. Such trusses are similar to the assemblage accounting for horizontal bending of the wall (Fig. 6a). However, their Young's modulus was calculated by calibrating the period of the modelled wall with the period of the first natural mode of vibration measured experimentally using random vibration tests (Table 3).

The calibrated period of the first natural mode of vibration of the numerical models is compared with those corresponding to the limiting numerical scenarios i.e. assuming fully-fixed (*FF*) and simply-supported (*SS*) conditions at the vertical edges along with experimentally measured values (Table 3) in Fig. 9. The values of stiffness that had to be adopted for the edge trusses to obtain the calibrated periods corresponded to E_{hb} values calculated (as per equation (6)) using 0.6–0.9 E_{xx}. Here, E_{xx} refers to the homogenized elastic stiffness values for each wall (reported in the following section in Table 4). As previously described, CS-005-RR was the only specimen for which three different methods of restraint was used. Thus, for the sake of simplicity, full-fixity on both vertical and horizontal edges is assumed. Consequently, the numerical period is slightly lower (~5%) than the experimental one. As regards CSW-000-RF, a reinforced concrete lintel was present above the window, which was not modelled. Thus, the edge trusses for CSW-000-RF were not calibrated against its measured period and the wall was modelled by simply creating an opening in the calibrated model of CS-000-RF.

4.2. Material properties

Material properties need to be defined at the *meso*-scale during the homogenization process at the RVE level. For all three sets of URM walls analysed the elastic homogenized parameters (E_{xx}, E_{yy}, G_{xy}) are summarised in Table 4 while the associated *M*- κ curves (section 3.2) are provided in Fig. 10. Note that similar E_{xx} values were obtained for both the WU-SJ batches. This is expected since horizontal bending for WU-SJ cases is controlled by units and the same units were used for both batches.

Material non-linearity is lumped on the interfaces and the multi-surface plasticity model by Lourenço and Rots [84] was used (Fig. 3c). For the SU-WJ masonry (Fig. 3a), interface elements were placed only at the unit-mortar (U-M) interface. For the WU-SJ masonry (Fig. 3b), an additional interface (U-U) was placed at the mid-length of the unit to simulate the splitting of units. The material properties required as input for the BVP at a *meso*-scale were defined taking into account the data available from the mechanical characterization tests and provided in Table 2. It is to be noted that the adopted properties do not refer (in some cases) to the experimental mean values due to numerical calibration. Yet, it may be highlighted that the calibration was developed by varying the material properties values, through a trial and error approach, within the bounds of the experimentally measured C.o.V to achieve good agreement in terms of the progression of damage, load capacity and the corresponding displacement. Both U-M and U-U interfaces properties are summarised in Table 5 for all batches to ensure reproducibility of the reported results. An exponential softening has been assumed for both tension and shear modes. Under a compression mode, both hardening and softening have been assumed: the hardening onset occurs for a stress that is three times lower than the compressive strength, and the softening branch is defined by a parabolic law. For all the considered modes, softening is controlled by fracture energy terms, which are reported in Table 5 ($G_f^{I.t}$ in tension, G_f^{II} in shear and $G_f^{I.c}$ in compression, respectively). These have been assumed following values reported in the literature [105].

The only material property beyond the variability exhibited by the mechanical characterisation was the cohesion (f_{v0}) assigned to the U-M

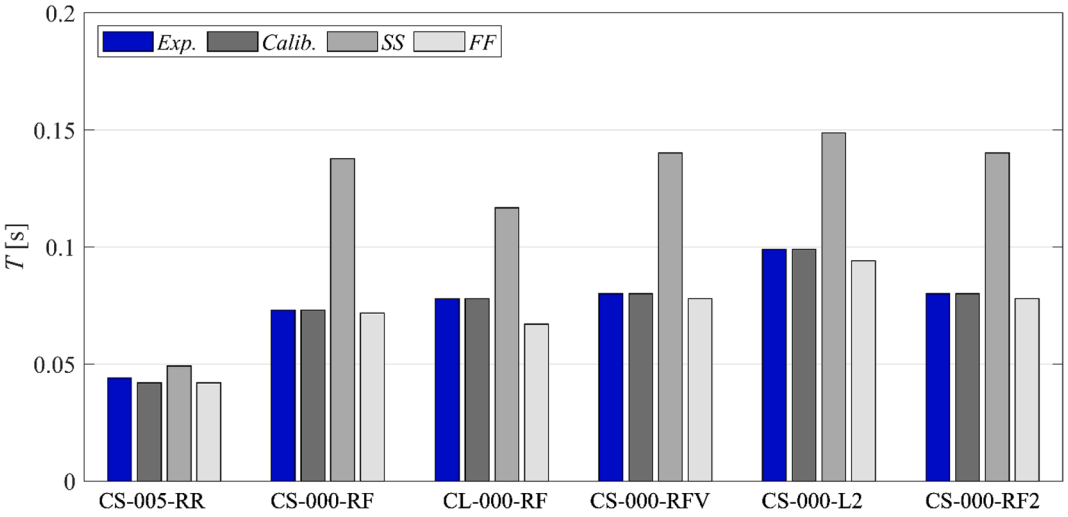

Fig. 9. Comparison of the period of the first natural mode of vibration obtained with the numerical models of the walls: calibrated (*Calib.*) vs. limiting scenarios of restraint at the vertical edges (*FF*: fully fixed and *SS*: simply-supported) along with experimentally measured values (*Exp.*)

Table 4
Homogenized elastic parameters adopted for all the URM batches analysed.

URM batches	Masonry (composite)			Brick units		Mortar joints	
	E_{xx} [MPa]	E_{yy} [MPa]	G_{xy} [MPa]	E_u [MPa]	G_u [MPa]	E_{mj} [MPa]	G_{mj} [MPa]
WU-SJ (CS) Graziotti *et al.* [25]	4834	4591	1742	5000	2000	3600	1385
SU-WJ (CL) Graziotti *et al.* [25]	10,806	5841	2698	20,000	9090	1300	580
WU-SJ (CS) Sharma *et al.* [26]	3234	3079	1048	5000	2000	700	269

Table 5
Material properties adopted for the interface elements for all batches of URM analysed to obtain the calibrated experimental response.

	Graziotti *et al.* [25]			Sharma *et al.* [26]	
	WU-SJ (CS)		SU-WJ (CL)	WU-SJ (CS)	
	U-M	U-U	U-M	U-M	U-U
Tensile Strength [MPa]	0.62	2.20	0.25	0.34	2.20
$G_f^{I,t}$ [N/mm]	0.03	0.03	0.02	0.02	0.03
Cohesion [MPa]	0.81	1.50	0.34	0.81	1.50
Friction coefficient [tan]	0.46	0.46	0.57	0.46	0.46
Dilatation coefficient [tan]	0.36	0.36	0.36	0.35	0.36
Residual Friction coefficient [tan]	0.27	0.27	0.27	0.27	0.27
G_f^{II} [N/mm]	0.05	0.05	0.03	0.05	0.05
Compressive strength f_c [MPa]	8.49	15.31	17.41	1.39	15.31
$G_f^{I,c}$ [N/mm]	0.50	1.00	1.00	0.40	1.00

interface for the WU-SJ (CS) masonry tested by Sharma *et al.* Since the f_{v0} of the U-M interface has little significance in the strength of WU-SJ URM (being controlled primarily by the U-U interface), the assumed value is equal to the one measured for WU-SJ URM by Graziotti *et al.* [25]. The value adopted can also be justified by the much higher torsional shear strength (the governing mode of shear in walls under OOP two-way bending) that was experimentally measured; when testing masonry couplets under torsional shear using a novel mechanical characterization test in [25].

4.3. Numerical vs. Experimental results

The numerical results are compared next with the experimental data. The comparison is given in terms of the progression of damage and load–displacement (capacity) curve. Numerically, the load–displacement curve was calculated from the pushover analyses by plotting the sum of reaction forces at all restrained nodes of the numerical model vs. displacement at a specified node. Experimental time-histories of inertial forces associated with the tested walls were computed by multiplying the acceleration recorded by accelerometers with a tributary mass assigned to them. To facilitate the comparison with the numerically obtained results, both positive (towards the return walls) and negative (away from the return walls) [25] experimental load–displacement hysteresis curves are plotted in the positive quadrant. Also, all the tested specimens were significantly instrumented [27,28] and experimental displacements were directly measured at the nodes where the numerical load–displacement (capacity) curves are plotted using appropriate instrumentation i.e. potentiometers and optical measurement systems. Numerically, the progression of damage was tracked by plotting the damage scalar (d) of the deformable trusses to which the CDP model (Fig. 7) had been assigned. Special attention is given to the numerical identification of mechanisms that leads to the development of the peak load of the walls.

4.3.1. Weak unit- strong joint (WU-SJ) walls

Weak Unit-Strong Joint (WU-SJ) walls constitute the majority of the tested specimens tested in [25] and [26]. A total of three specimens: CS-000-RF from [25], CS-000-RFV and CS-000-RF2 from [26], had been tested with three edges restrained and the top edge kept free. All three specimens had exhibited a very similar response [26]. These specimens exhibited a brittle behaviour i.e. the onset of cracking and the collapse took place over a very limited number of loading cycles. Fig. 11b demonstrates the experimental failure mechanism of these walls. Damage appeared in the form of line cracking, involving the splitting of units, at the centre of the wall and their connection with the return walls. Load capacity started decreasing when all the latter cracks are formed, which subsequently led to the overturning and collapse of the wall about a horizontal hinge surface. Such a surface is defined by a horizontal line

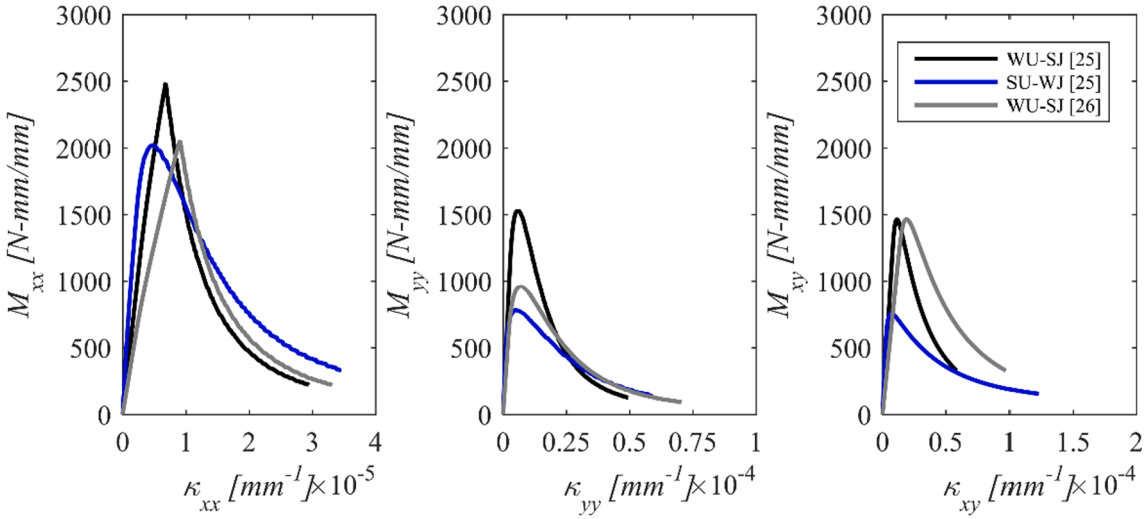

Fig. 10. Moment curvature *(M-κ)* curves associated with the three batches of URM analysed.

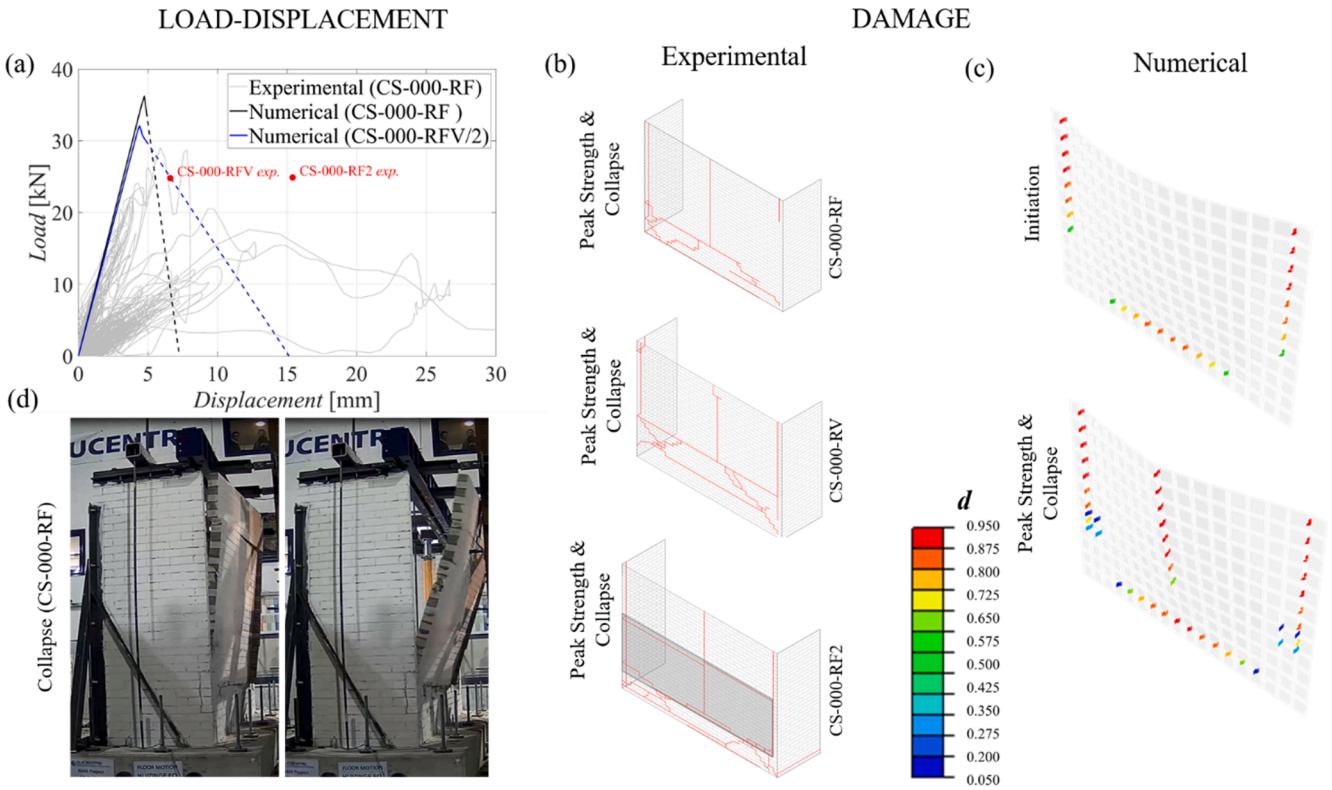

Fig. 11. Comparison between the experimental and numerical responses for WU-SJ walls restrained on all three sides and free at the top (i.e. CS-000-RF [25], CS-000-RFV [26] and CS-000-RF2 [26] in Table 1): (a) experimental and numerical load–displacement behaviour; (b) experimental progression of damage; (c) numerical progression of damage; and (d) snapshots of the experimental collapse of CS-000-RF.

crack as given in Fig. 11b, whose location in the height of the panel is directly dependent on the length of the vertical line cracks. It is to be noted here that for the case of CS-000-RF2, the complete overturning of a portion of the wall (marked in grey in Fig. 11c) was prevented by the presence of wire-potentiometers that were still recording when it collapsed [26]. Very similar load capacity values (Fig. 11a) were exhibited by all the three walls, despite the relatively lower mechanical properties of the mortar joints of specimens CS-000-RFV and CS-000-RF2 when compared to CS-000-RF (Table 2). Peak load capacity was also reached at a similar displacement (around 6 mm) by both CS-000-RF and CS-000-RFV. In converse, the CS-000-RF2 registered a displacement of 15 mm at the peak strength of the curve, this higher value being attributed in Sharma *et al.* [26] to the even faster progression of damage, as compared to CS-000-RF and CS-000-RFV.

A promising agreement was found between the numerical and experimental results concerning the damage observations. The numerical damage onset took place in the form of horizontal cracking near the base of the wall and through vertical line cracking in the proximity of the vertical edges (Fig. 11c). This was followed by the development of a vertical line crack in the centre of the panel when the peak load capacity was attained. The experimental load–displacement curve is given here for the CS-000-RF only (see Fig. 11a) due to the similarity of the responses between the studied walls. Nonetheless, the peak load capacity and the corresponding displacement are also plotted for CS-000-RFV and CS-000-RF2. Fig. 11a shows that a good agreement was observed in terms of peak load capacity between the numerical and experimental data with an average relative difference of approximately 20%. Although acceptable, note that such average relative difference is accentuated since the numerical model catches the entire height of the tested wall panel to be involved in the failure mechanism. Experimentally, the height of the panel involved in the failure mechanism was always shorter, presumably due to intra-wall variability of material properties [28].

The displacement at which peak load capacity occurred was slightly underestimated. For these walls, displacements (both experimental and numerical) are plotted at the centre of the free top edge. It is to be noted here that collapse cannot be explicitly captured using the numerical model due to the intrinsic brittle response being simulated and associated typical numerical convergence issues. Still, one may assume that numerically collapse occurs when cracks join to form a mechanism, i.e. when the vertical cracks met the horizontal crack at the base of the panel. The post-collapse part (dashed line) of the numerical load–displacement curve in Fig. 11a was, therefore, assumed by the authors through linear extrapolation. It is also to be noted that CS-000-RFV was subjected to a simultaneous OOP and vertical excitation. Vertical dynamic excitation was not considered since applying it through a static fashion via a ‘push-down’ strategy would be arguable especially when simultaneously applying a ‘push-over’ load. Nevertheless, it is to be noted that the effect of the vertical excitation seemed negligible as: the failure mode was controlled by the splitting of units (as expected in a WU-SJ type of masonry); and due to the difference in the frequency content of the applied excitations [26]. Regarding the CSW-000-RF wall, it has the same dimensions than CS-000-RF but an eccentric opening is present. The RC lintel above the opening was neglected in the modelling. Despite such a simplification, a particularly good agreement was again observed between the numerical and experimental results. Peak load capacity in both experimental and numerical scenarios, was attained when vertical line cracks appeared at the connection with the left return wall and the upper right extremity of the opening. The initiation of a horizontal crack was also observed both experimentally and numerically at the lower left corner of the opening (Fig. 12b,c). At the end of experimental testing, CSW-000-RF was heavily damaged with negligible residual capacity towards both OOP or vertical in-plane loads (Fig. 12d) [25]. Although extensive cracking was documented at the end of testing, Graziotti *et al.* [25] noted that the failure mechanism was triggered by a diagonal cracking that developed from the left edge of the opening to the

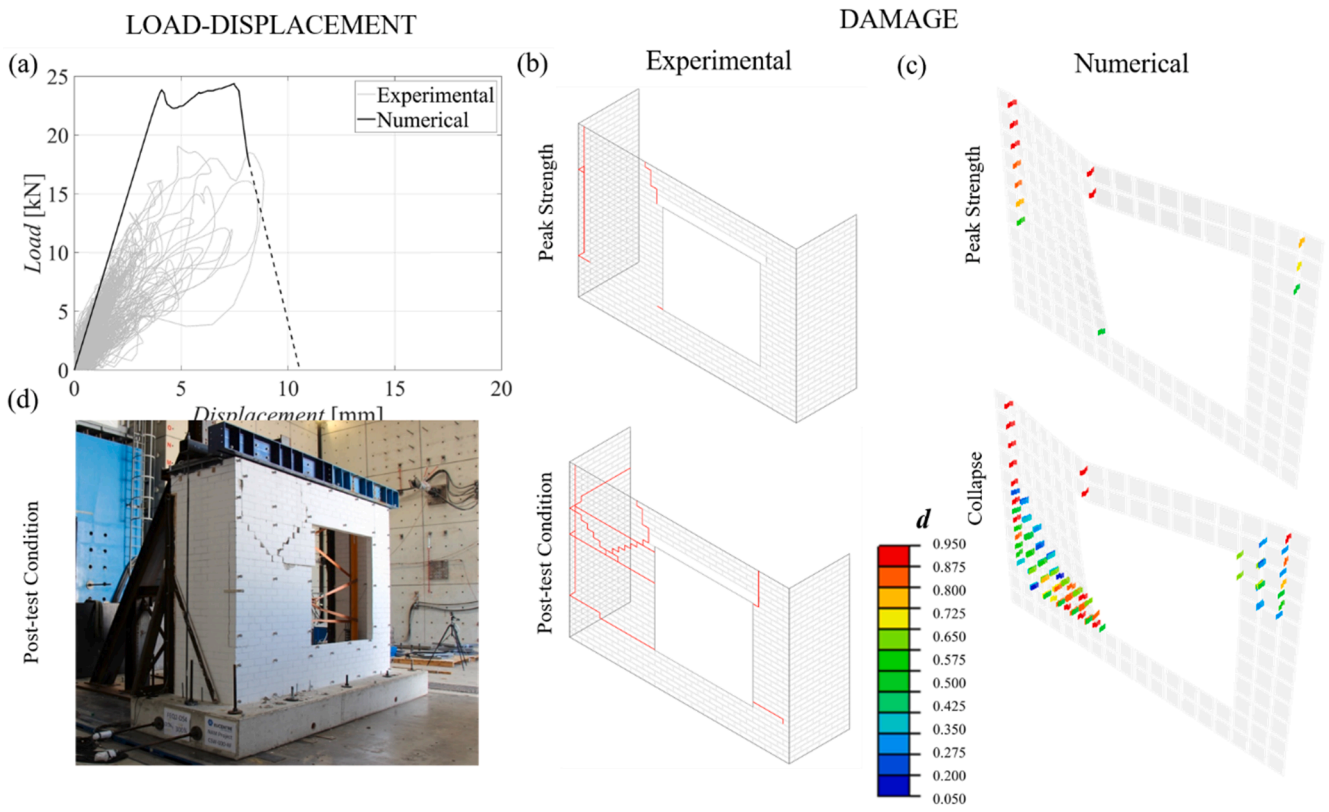

Fig. 12. Comparison between the experimental and numerical responses for the WU-SJ walls restrained on all three sides and free at top and with an eccentric opening (i.e. CSW-000-RF [25] in Table 1): (a) experimental and numerical load–displacement behaviour; (b) experimental progression of damage; (c) numerical progression of damage; and (d) CSW-000-RF at the end of testing.

left return wall (see Fig. 12e). This was also captured by the numerical model, though at a slightly lower height as shown in Fig. 12c.

Specimen CS-000-L2 was tested in Sharma *et al.* [26] with adjacent horizontal and vertical edges free. Even for this configuration, the initiation of cracking and the collapse for the specimen occurred simultaneously. Again, the onset of damage was in the form of a line crack at the connection with the return wall connection, extending from the top edge to mid-height of the panel. This was immediately followed by the overturning of the cracked portion of the panel (Fig. 13b and d). Numerically, it was observed that the onset of damage took place in the proximity of the free edge near the base of the wall (Fig. 13c). However, both the numerical peak load capacity and the collapse of the specimen were developed in the same fashion as observed experimentally, i.e. overturning and the collapse of the wall after the formation of line cracks at the restrained vertical edge. The peak load capacity was estimated quite well by the model, with a relative difference of just 6% with respect to what was experimentally measured. Regarding specimen CS-005-RR [25], it is impossible to numerically attain the unsymmetrical crack observed at the onset of experimental damage (Fig. 14b). Nevertheless, both numerical and experimental mechanisms were very similar. An excellent agreement could also be observed in terms of peak load capacity as well as the associated displacement (Fig. 14a).

4.3.2. *Strong unit- weak joint (SU-WJ) wall*

A single SU-WJ wall (CL-000-RF) with three edges restrained and the top edge free was tested by Graziotti *et al.* [25]. Initiation of damage for this wall took place in the form a horizontal crack near the base of the wall (Fig. 15b). Although the wall partially collapsed onto the shake-table (Fig. 1a and Fig. 15d), the mechanism leading to the development of its peak load capacity was reproduced by a careful examination of a video recording of the test in [25] (Fig. 15b,d). The exact progression of damage was reproduced also by the model (Fig. 15c). Again, a good agreement with experimental measurements was observed in terms of peak load capacity with a relative difference of 2%.

The numerical strategy was observed to give results in excellent agreement with the experimental ones for both the WU-SJ and SU-WJ URM walls, both in terms of damage evolution and capacity. Generally, the numerical displacement at which peak load capacity was attained was consistently slightly under-estimated. However, this is presumably a result of the cyclic degradation of the strength and stiffness that occurred experimentally since incremental dynamic tests had been performed. In contrast, the numerical analyses adopted a pushover-based approach and such degradation phenomena were disregarded owing to the monotonic nature of the loading.

5. Response prediction of untested URM wall configurations

The numerical models presented in the previous section were used to predict the behaviour of SU-WJ walls in untested configurations (with respect to the reference experimental campaigns [25,26]). The numerical results were compared with state-of-the-art analytical methods [67,68] based on the virtual work method that had been already validated for the tested WU-SJ walls in [25,26].

5.1. *Numerical response prediction for untested Strong Unit- Weak joint (SU-WJ) walls*

Numerical analysis was performed on SU-WJ walls restrained on all four edges (N-CL-000-RR analogous to CS-005-RR in [25]) and restrained on only two-adjacent edges (N-CL-000-L2 analogous to CS-000-L2 in [26]) (Fig. 16b). It is important to note here that conversely to CS-005-RR [25], no pre-compression of 0.05 MPa was assumed on the top horizontal edge and the same reflects in its name i.e. N-CL-000-RR with N denoting that the results are numerical. This was assumed to use

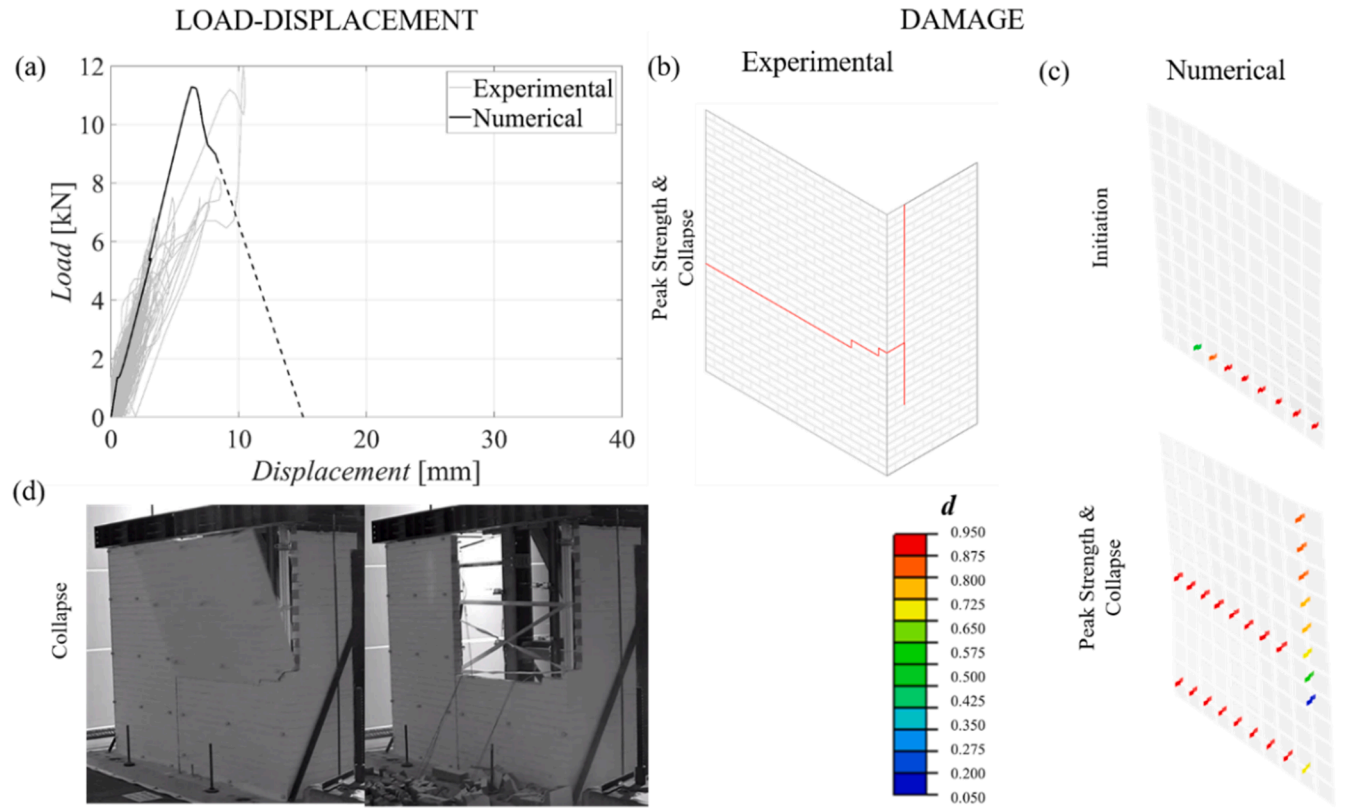

Fig. 13. Comparison between the experimental and numerical response for the WU-SJ wall restrained on all two adjacent sides only (i.e. CS-000-L2 [26] in Table 1): (a) experimental and numerical load–displacement behaviour; (b) experimental progression of damage; (c) numerical progression of damage; and (d) snapshots of the experimental collapse of CS-000-L2.

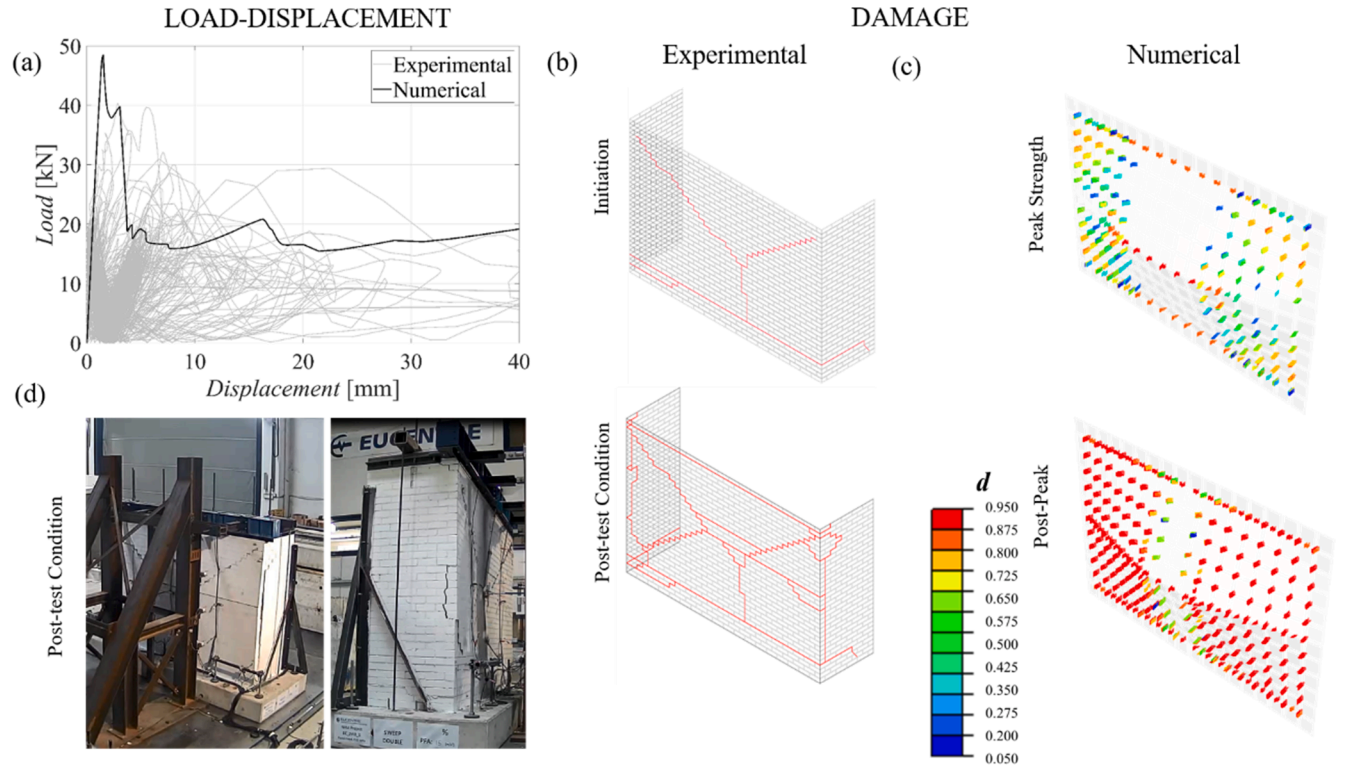

Fig. 14. Comparison between the experimental and numerical response for the WU-SJ walls restrained on all four sides (i.e. CS-005-RR [25] in Table 1): (a) experimental and numerical load–displacement behaviour; (b) experimental progression of damage; (c) numerical progression of damage; and (d) CS-005-RR at the end of testing.

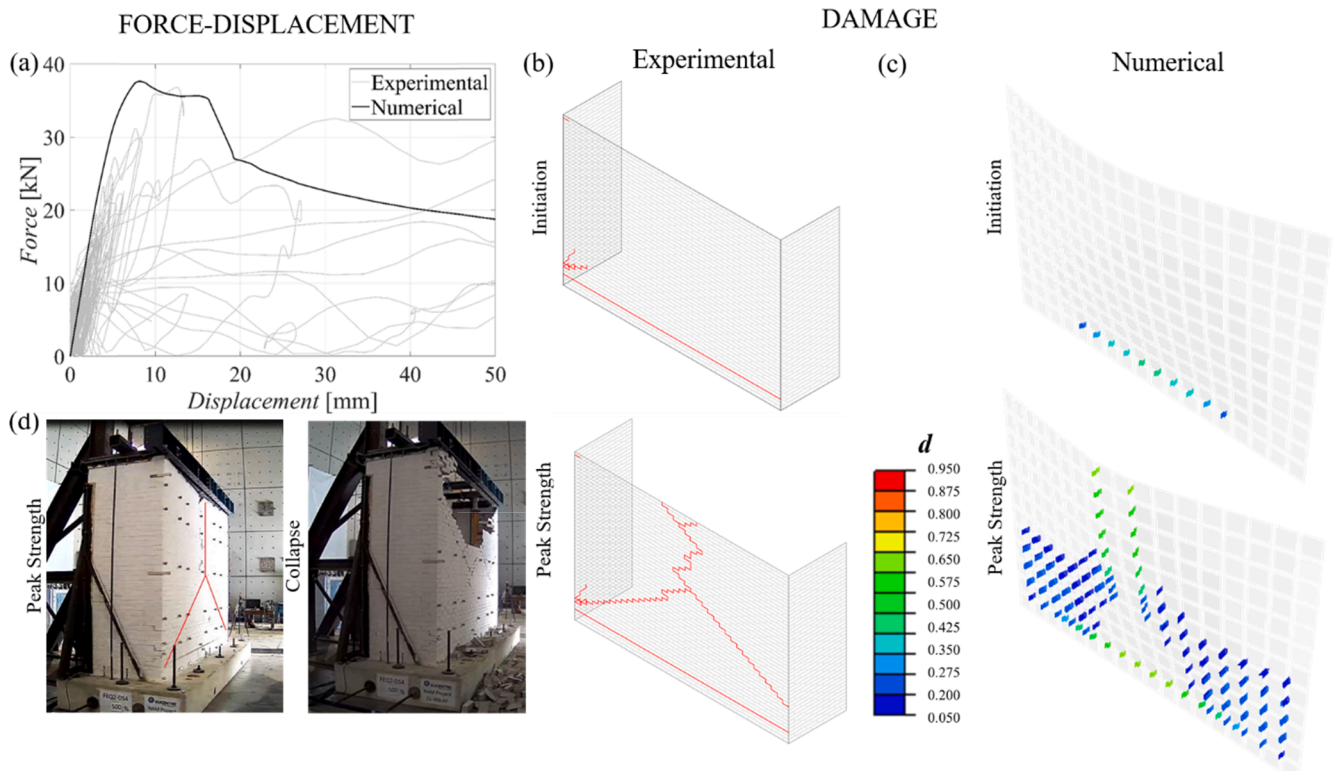

Fig. 15. Comparison between the experimental and numerical response for SU-WJ walls restrained on all three sides and free at the top (i.e. CL-000-RF [25] in Table 1): (a) experimental and numerical load–displacement behaviour; (b) experimental progression of damage; (c) numerical progression of damage; and (d) snapshots of the experimental collapse of CL-000-RF.

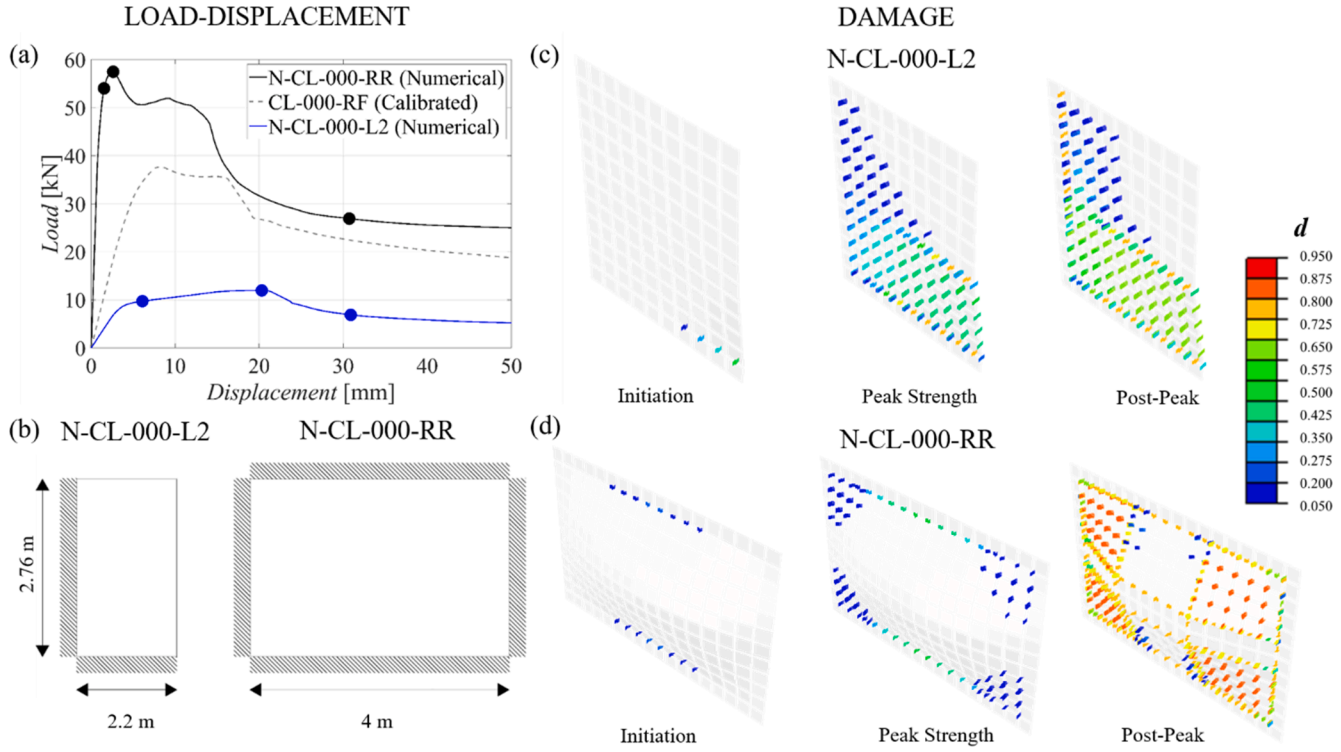

Fig. 16. Numerical predictions for the SU-WJ walls hitherto untested using the calibrated material properties of the SU-WJ specimen (i.e. CL-000-RF [25] in Table 1): (a) numerical load–displacement behaviour; (b) dimensions and boundary conditions of the walls considered numerically; (c) numerical progression of damage for N-CL-000-L2; and (d) numerical progression of damage for N-CL-000-RR.

exactly the same material properties derived via the calibration of the CL-000-RF specimen response. As no experimental information was available on the fundamental mode of vibration period of these walls, an intermediate fixity at vertical edges was not assumed. Instead, all the supported edges were fixed. Adopting such an assumption also allows a fair comparison with state-of-the-art analytical methods.

The failure mechanisms predicted for both N-CL-000-L2 and N-CL-000-RR follows the expected ones i.e. the standard failure mechanisms for URM walls under OOP two-way bending [104] (see Fig. 17). The significant differences found in terms of stiffness and load capacity values observed for the N-CL-000-L2, CL-000-RF and N-CL-000-RR are explained by the different boundary conditions. However, an important remark may be addressed concerning the SU-WJ walls as compared to their WU-SJ counterparts. Walls belonging to the SU-WJ typology presents a much more diffused damage for the peak load capacity value (Fig. 15c, Fig. 16c and Fig. 16d). Regarding WU-SJ walls, the damage was highly localised and the associated values for the damage scalars (d) for the peak load capacity case are much higher (Fig. 11c, Fig. 12c and Fig. 14c). This is also consistent with the expected behaviour since the failure of WU-SJ masonry is primarily dominated by the splitting of units, a mechanism far more brittle compared to the torsional shear failure of bed joints that controls the strength of SU-WJ masonry.

5.2. Comparison between numerical and analytical approaches

Analytical approaches and design rules remain the most widely and commonly used methods in engineering practice because of their simplicity. State-of-the-art analytical methods to assess the strength of URM walls in two-way bending are based on the virtual work method, which has been codified in a tabular form by Lawrence and Marshall [67] and adopted by the Australian normative for URM structures (AS 3700 [106]). The virtual work method requires the knowledge of the failure mechanism associated with a wall to calculate the associated load capacity. In this context, the codified method [67,68] implicitly assumes a standard failure mechanism for the wall under two-way OOP bending and based on its geometry and boundary conditions from those shown in Fig. 17.

Assuming a standard failure mechanism, the method calculates the peak load capacity (kN) of a URM wall under OOP two-way bending as per equation (8):

$$Peak\ Load\ Capacity = \frac{2a_f}{g \times L_d{}^2}\left(k_1 M_h + k_2 M_d\right) \times L \times H \tag{8}$$

in which k_1, k_2 and a_f are coefficients dependent on the associated failure mechanism and can be obtained in Lawrence and Marshall [67] as well as AS 3700 [106]. L_d is the effective length of the wall which depends on its boundary conditions and presence or absence of an opening; L and H are, respectively, the length and height of the wall being assessed while g is the acceleration due to gravity. The only material strength related terms in Equation (8) are M_h and M_d which denote moment capacities associated with horizontal and diagonal bending per unit crack length. In this context, it is important to note that the coefficient k_1 multiplied with M_h incorporates another numerical factor given by R_f, which allows the consideration of weighted contributions of the horizontal bending at the vertical supports of the wall. R_f ranges between 0 and 1 with a value of $R_f = 1$ implying a full-moment transmission.

Several approaches are available in literature to compute M_h and M_d. The equations for M_h and M_d in AS 3700 [106] are empirical and dimensionally inconsistent and, therefore, disregarded in this work. However, significant improvements to these equations were carried out by Willis [69] and Vaculik [104]. These improvements resulted in rational mechanical equations to calculate both M_h and M_d that are reported next:

$$M_d = \frac{\sin\varphi}{h_u + t_j}\left[(\sin\varphi)^3\ \tau_u\ k_b\ 0.5\ \left(l_u + t_j\right)\ t_u{}^2 + (\cos\varphi)^3\ \left(f_{mt} + \sigma\right)\ \frac{0.5\ \left(l_u + t_j\right)\ t_u{}^2}{6}\right] \tag{10}$$

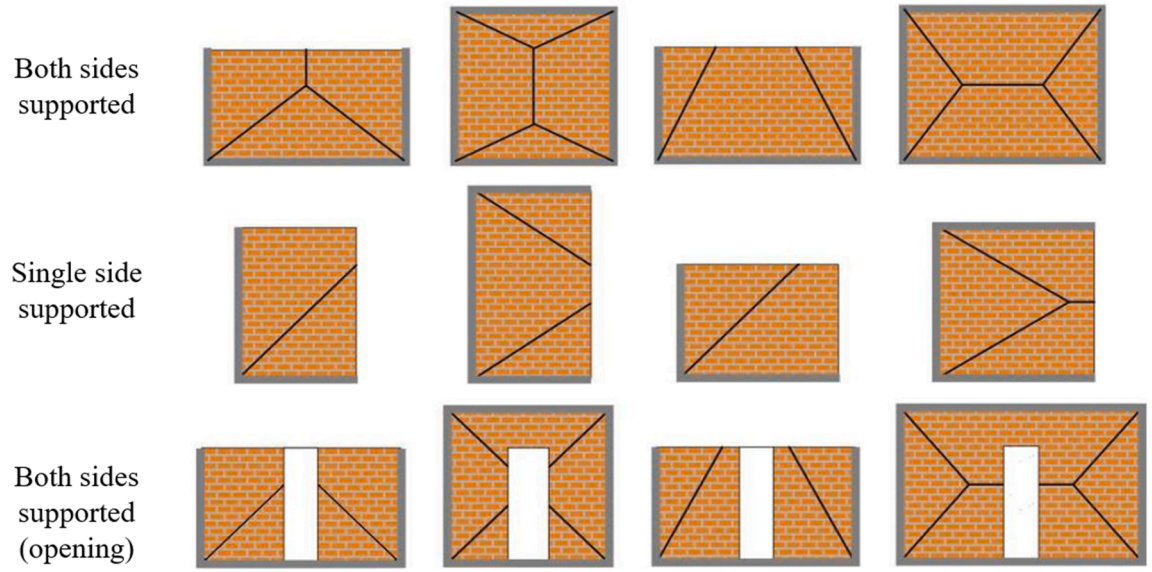

Fig. 17. Failure mechanisms under out-of-plane two-way bending corresponding to various wall configurations assumed by the codified form of the virtual work method (reproduced from [104]).

$$M_h = min\begin{cases} \frac{1}{2(h_u + t_j)}\left[(f_{ut} - \nu\,\sigma)\,h_u\frac{t_u^2}{6}\right](WU - SJ) \\ \frac{1}{h_u + t_j}\left[\tau_u\,k_b\,0.5\,(l_u + t_j)\,t_u^2\right](SU - WJ) \end{cases} \quad (9)$$

in which l_u, h_u and t_u are the length, height and thickness of a brick unit; t_j is the thickness of a mortar joint; φ is the assumed global slope of a stepped diagonal crack calculated from unit geometry as $2(h_u + t_j)/(l_u + t_j)$ implying that diagonal stepped cracks follow the natural slope dictated by the size of units and their bond (overlap); f_{mt} is the flexural tensile strength of masonry as a composite; f_{ut} the flexural tensile strength of a brick unit, σ is the vertical pre-compression at mid-height of the wall and ν is the Poisson's ratio of masonry which was taken as 0.2 here. The parameter τ_u denotes the ultimate torsional shear stress in a masonry bed joint, while k_b multiplied with it is a numerical factor whose value depends on the distribution of shear stresses in the bed joint when peak torsional shear response is attained.

Different approaches can be adopted to calculate τ_u. The state-of-the-art currently in literature is an empirical relationship proposed by Willis [69], in which $\tau_u = 0.9\sigma + 1.6f_{mt}$, f_{mt} being the flexural tensile strength of masonry [75]. Willis also proposed adopting a value of 0.208 for k_b, implying an elastic shear stress distribution when peak torsional shear response is attained. It is interesting to note here that f_{mt} controls the strength of the vertical bending and has residual importance for horizontal bending. Horizontal cracks, due to vertical bending, were observed to form much before the attainment of peak load capacity in all tested/modelled specimens and are unlikely to contribute significantly to peak load capacity. The influence of vertical bending/horizontal cracks is not taken into account for the adopted analytical approaches because of the same observation by other experimental studies [102,103]. Shortcomings of this relationship were also highlighted in the reference experimental studies and consequently it was not considered in this work. Instead, torsional shear strength values that were measured experimentally by Graziotti *et al.* [25] in the reference experimental campaign was used to perform the calculations reported in Table 6, in order to minimize uncertainities associated with calculating this parameter (i.e. by relationships proposed by [69,107]). The torsional shear strength of the URM used to construct CL-000-RF was experimentally measured as $\tau_u = 1.55\sigma + 1.07$ from torsional shear experiments performed on masonry couplets, assuming again an elastic distribution of stress when peak torsional shear response is attained i.e. $k_b = 0.208$. Moreover, since full-moment transfer was assumed at the vertical edges in the numerical models of N-CL-000-RR and N-CL-000-L2, a value of $R_f = 1$ was adopted for their analytical calculations. In the case of CL-000-RF, a value of $R_f = 0.6$ was adopted as edge trusses having E_{hb} values corresponding to $0.6E_{xx}$ (see section 4.1) had been used to obtain the calibrated experimental response.

A good agreement can be observed in Table 6 between numerical and analytical results for CL-000-RF and N-CL-000-RR. However, in the case of N-CL-000-L2, the analytical approach overestimates the peak load capacity by almost 60%. While further research is also warranted into understanding the torsional shear strength of bed joints τ_u, another aspect that needs to be investigated is the underlying assumptions of the analytical formulation that was applied here. The applied method assumes that peak moment capacities of all diagonal and horizontal cracks of the assumed failure mechanism (Fig. 17) are reached simultaneously. This assumption seems reasonable for the tested/modelled WU-SJ walls, considering the simultaneous appearance of localized cracks associated with high values of damage (d) observed for them. However, in the case of the numerically modelled SU-WJ walls, it can be appreciated from Fig. 15f, Fig. 16b,d that peak load capacity is associated with more diffused yet lighter damage (lower d values) throughout the panel. In case of specimen N-CL-000-L2 (Fig. 16a), the initiation of damage occured much before the attainment of peak load capacity, leading to a possible accentuation of such effects. It is interesting to note that a similar difference in the cracking behaviour i.e. localized high damage vs. diffused lower damage of WU-SJ (CS brick) and SU-WJ (CL brick) URM walls under in-plane loading was also observed experimentally by Korswagen *et al.* [108].

Table 6
Comparison between the numerical and analytical predictions for the peak load capacity of specimens.

	Peak Load Capacity			Difference
	Experimental [kN]	Numerical [kN]	Analytical [kN]	(Analytical w.r.t. Numerical)
CL-000-RF	36.80	37.63	38.26	+1.67%
N-CL-000-RR	–	57.48	53.96	−6.12%
N-CL-000-L2	–	9.72	15.62	+60.70%

In the case of WU-SJ walls, good agreement in [25,26] was also found for the analytical methods when using a value of $R_f = 0.5$, as recommended by Griffith and Vaculik [71]. However, it was remarked in Sharma *et al.* [26] that the assumption of $R_f = 0.5$, meaning that 50% of the horizontal bending moment capacity at vertical edges contributing to the peak load capacity of the wall could give a good fit as a result of all cracks not reaching their full capacity simultaneously. Conversely, AS 3700 [106] and Griffith and Vaculik [71] suggest that $R_f = 0.5$ is presumably indicative of a boundary condition intermediate between a simply supported ($R_f = 0$) and completely fixed ($R_f = 1$) scenario being realized at the restrained vertical edges. The numerical models seem to indicate the same as Sharma *et al.* [26]: good agreement between numerical and experimental results for WU-SJ walls was achieved adopting an almost fully-fixed condition at the vertical edges (Fig. 9).

Such observations highlight several possible interesting future applications of the proposed modelling approach. For SU-WJ walls, the load capacity is visibly controlled by both horizontal and diagonal bending resulting in vertical and diagonal stepped cracks, respectively. As already noted, these cracks develop progressively over the load–displacement behaviour of the walls. Consequently, different contributions are expected from the horizontal and diagonal bending components towards the wall capacity. While this is implicitly accounted for by the proposed numerical model, it is disregarded by the analytical approaches used here. Considering the low computational effort associated with the adopted numerical strategy [109], extensive parametric analysis could be performed to evaluate their separate weighted contributions and, accordingly, to improve the latter analytical methods. Such improvements should be directed towards calculating factors incorporated in the terms k_1 and k_2 in equation (8) accounting for weighted contributions of M_h and M_d. Another interesting application may be the investigation of the diagonal bending contribution to the capacity of WU-SJ walls within certain configurations. WU-SJ walls, in certain configurations (Fig. 11, Fig. 12 and Fig. 13), tend to exhibit only damage corresponding to horizontal bending at the attainment of peak load capacity; this was seen both at numerical and experimental levels ([2526]). In this context, it is interesting to note that the virtual work method was explicitly applied taking into account experimentally observed failure mechanisms instead of the standard ones assumed by the codified form in Graziotti *et al.* [25]. An even better agreement as compared to the codified virtual work method (implemented here) with experimentally measured peak load capacities was achieved by neglecting the contribution of diagonal cracks.

6. Concluding remarks

A non-linear discrete homogenized-based strategy for modelling the

out-of-plane (OOP) two-way bending response of unreinforced (URM) brick masonry walls has been presented. As per the adopted strategy, walls are modelled as an assemblage of rigid plates interconnected by a system of non-linear deformable trusses. The material input for the non-linear deformable trusses is derived from a homogenization process. The numerical strategy was validated against the results of full-scale dynamic experiments on URM walls. While similar strategies have been presented before, this study represents one of the first instances in which such a strategy has been validated against full-scale shaking table experiments. The numerical models exhibited good agreement with experimental results in terms of peak load capacity and observed damage: both progression as well as the final failure mechanism.

A majority of the walls tested in the reference experimental campaigns corresponded to a "Weak Unit- Strong Joint" (WU-SJ) masonry which exhibits a vertical crack passing through the brick units and head joints under pure horizontal bending. Considering the good performance of the numerical strategy, calibrated mechanical parameters were used to study the behaviour of "Strong Unit- Weak Joint" (SU-WJ) masonry walls in experimentally untested configurations aiming to complete the database of information. Here, SU-WJ refers to URM which exhibits a stepped crack passing through head joints and half a bed joint under pure horizontal bending. For the WU-SJ walls, high damage was observed in localized regions of the wall when peak load capacity was attained. In contrast, the models of the SU-WJ walls presented much lower diffused damage at peak load capacity. Another observation made numerically, as well as experimentally during the reference incremental dynamic testing campaigns, was the non-occurrence of diagonal cracks at peak load capacity for WU-SJ walls free at their top edge.

State-of-the-art analytical methods to assess the load capacity of URM walls in two-way bending based on the virtual work method were also applied for the numerically analysed SU-WJ walls. The numerical strategy predicts higher peak load capacities as compared to the analytical methods. This is attributed possibly to the diffused cracking observed for the SU-WJ walls when peak load capacity is attained since it is precluded by analytical methods. While analytical methods remain widely used in practice because of their simplicity and ease of use, a big shortcoming associated with the state-of-the-art analytical methods applicable for OOP two-way bending is that the failure mechanism needs to be known *a priori*. The formulation also needs to be derived for every individual mechanism, load case and boundary conditions. The load capacity and failure mechanism can be predicted without such limitations by the adopted modelling approach. This is of prime importance especially in the context of retrofit and repair.

A natural extension of the work carried out in this study is implementing the same modelling approach to model the dynamic behaviour of the tested URM walls in OOP two-way bending. However, the non-linear static analyses performed in this work result in a clearer characterisation of the load–displacement behaviour of the walls when compared to dynamic analyses. Considering this and the low computational effort associated with the model, these analyses can be performed parametrically to improve the state-of-the-art virtual work method based analytical approaches.

CRediT authorship contribution statement

S. Sharma: Conceptualization, Methodology, Investigation, Validation, Data curation, Writing - original draft, Writing - review & editing. **L.C. Silva:** Conceptualization, Methodology, Software, Validation, Data curation, Writing - original draft, Writing - review & editing. **F. Graziotti:** Conceptualization, Methodology, Data curation, Investigation, Writing - original draft, Supervision. **G. Magenes:** Conceptualization, Methodology, Validation, Writing - original draft, Resources, Supervision. **G. Milani:** Conceptualization, Methodology, Software, Visualization, Writing - original draft, Writing - review & editing, Supervision.

Declaration of Competing Interest

The authors declare that they have no known competing financial interests or personal relationships that could have appeared to influence the work reported in this paper.

Acknowledgements

This article reports studies performed as a part of the "Study of the vulnerability of masonry buildings in Groningen" project at the EUCENTRE, undertaken within the framework of the research program for investigating the hazard and risk of induced seismicity in Groningen sponsored by the Nederlandse Aardolie Maatschappij BV. The authors would like to acknowledge the support of Paulo B. Lourenço and Maria Pia Ciocci towards realising this collaborative effort. Special thanks go to Panchami Goswami and Luca Grottoli for their help.

References

[1] Paulay T, Priestly MJN. Seismic Design of Reinforced Concrete and Masonry Buildings. Hoboken, NJ, USA: John Wiley & Sons, Inc.; 1992. doi:10.1002/9780470172841.
[2] Menon A, Magenes G. Definition of Seismic Input for Out-of-Plane Response of Masonry Walls: I. Parametric Study. J Earthq Eng 2011;15:165–94. https://doi.org/10.1080/13632460903456981.
[3] Moon L, Dizhur D, Senaldi I, Derakhshan H, Griffith M, Magenes G, et al. The demise of the URM building stock in Christchurch during the 2010–2011 Canterbury earthquake sequence. Earthq Spectra 2014;30:253–76. https://doi.org/10.1193/022113EQS044M.
[4] Page AW. The Newcastle Earthquake - Behaviour of Masonry Structures. Mason Int 1991;5:11–8.
[5] Penna A, Morandi P, Rota M, Manzini CF, da Porto F, Magenes G. Performance of masonry buildings during the Emilia 2012 earthquake. Bull Earthq Eng 2014;12:2255–73. https://doi.org/10.1007/s10518-013-9496-6.
[6] Oyarzo-Vera C, Griffith MC. The Mw 6.3 Abruzzo (Italy) earthquake of april 6th, 2009: On site observations. Bull New Zeal Soc Earthq Eng 2009;42:302–7.
[7] D'Ayala DF, Paganoni S. Assessment and analysis of damage in L'Aquila historic city centre after 6th April 2009. Bull Earthq Eng 2011;9:81–104. https://doi.org/10.1007/s10518-010-9224-4.
[8] Craig GM, K. LNT, Leonard WJ, Kevin D. Experimental Investigation of Unreinforced Brick Masonry Walls in Flexure. J Struct Eng 2004;130:423–32. doi:10.1061/(ASCE)0733-9445(2004)130:3(423).
[9] Simsir CC, Aschheim MA, Abrams DP. Out-of-plane dynamic response of unreinforced bearing walls attached to flexible diaphragms. Proc. 13th World Conf. Earthq. Eng., Vancouver, British Columbia, Canada: 2004.
[10] Penner O, Elwood KJ. Out-of-plane dynamic stability of unreinforced masonry walls in one-way bending: Parametric study and assessment guidelines. Earthq Spectra 2016;32:1699–723. https://doi.org/10.1193/011715EQS011M.
[11] Giaretton M, Dizhur D, Ingham JM. Dynamic testing of as-built clay brick unreinforced masonry parapets. Eng Struct 2016;127:676–85. https://doi.org/10.1016/j.engstruct.2016.09.016.
[12] Graziotti F, Tomassetti U, Penna A, Magenes G. Out-of-plane shaking table tests on URM single leaf and cavity walls. Eng Struct 2016;125. https://doi.org/10.1016/j.engstruct.2016.07.011.
[13] Lam NTK, Griffith M, Wilson J, Doherty K. Time-history analysis of URM walls in out-of-plane flexure. Eng Struct 2003;25:743–54. https://doi.org/10.1016/S0141-0296(02)00218-3.
[14] Sorrentino L, Masiani R, Griffith MC. The vertical spanning strip wall as a coupled rocking rigid body assembly. Struct Eng Mech 2008;29:433–53. https://doi.org/10.12989/sem.2008.29.4.433.
[15] Tomassetti U, Graziotti F, Penna A, Magenes G. Modelling one-way out-of-plane response of single-leaf and cavity walls. Eng Struct 2018. https://doi.org/10.1016/j.engstruct.2018.04.007.
[16] Godio M, Beyer K. Trilinear Model for the Out-of-Plane Seismic Assessment of Vertically Spanning Unreinforced Masonry Walls. J Struct Eng 2019;145:04019159. https://doi.org/10.1061/(ASCE)ST.1943-541X.0002443.
[17] Drysdale RG, Hamid AA, Baker L. Masonry Structures: Behavior and Design. Englewood Cliffs, New Jersey: Prentice-Hall; 1994.
[18] Vaculik J, Griffith MC, Hogarth B, Todd J. Out-of-plane flexural response tests using dry-stack masonry. Proc. Aust. Earthq. Soc. Conf., Mt Gambier, South Australia: 2004.
[19] Griffith MC, Vaculik J, Lam NTK, Wilson J, Lumantarna E. Cyclic testing of unreinforced masonry walls in two-way bending. Earthq Eng Struct Dyn 2007;36:801–21. https://doi.org/10.1002/eqe.654.
[20] Walsh KQ, Dizhur DY, Shafaei J, Derakhshan H, Ingham JM. In Situ Out-of-Plane Testing of Unreinforced Masonry Cavity Walls in as-Built and Improved Conditions. Structures 2015;3:187–99. https://doi.org/10.1016/j.istruc.2015.04.005.

[21] Restrepo Vélez LF, Magenes G, Griffith MC. Dry stone masonry walls in bending-Part I: Static tests. Int J Archit Herit 2014;8:1–28. https://doi.org/10.1080/15583058.2012.663059.

[22] Maccarini H, Vasconcelos G, Rodrigues H, Ortega J, Lourenço PB. Out-of-plane behavior of stone masonry walls: Experimental and numerical analysis. Constr Build Mater 2018. https://doi.org/10.1016/j.conbuildmat.2018.05.216.

[23] Damiola M, Esposito R, Messali F, Rots JG. Quasi-static cyclic two-way out-of-plane bending tests and analytical models comparison for URM walls. Proc. 10th Int. Mason. Conf., Milan, Italy: 2018.

[24] Vaculik J, Griffith MC. Out-of-plane shaketable testing of unreinforced masonry walls in two-way bending. Bull Earthq Eng 2018. https://doi.org/10.1007/s10518-017-0282-8.

[25] Graziotti F, Tomassetti U, Sharma S, Grottoli L, Magenes G. Experimental response of URM single leaf and cavity walls in out-of-plane two-way bending generated by seismic excitation. Constr Build Mater 2019;195:650–70. https://doi.org/10.1016/j.conbuildmat.2018.10.076.

[26] Sharma S, Tomassetti U, Grottoli L, Graziotti F. Two-way bending experimental response of URM walls subjected to combined horizontal and vertical seismic excitation. Eng Struct 2020;219:110537. https://doi.org/10.1016/j.engstruct.2020.110537.

[27] Tomassetti U, Grottoli L, Sharma S, Graziotti F. Dataset from dynamic shake-table testing of five full-scale single leaf and cavity URM walls subjected to out-of-plane two-way bending. Data Br 2019. https://doi.org/10.1016/j.dib.2019.103854.

[28] Sharma S, Grottoli L, Tomassetti U, Graziotti F. Dataset from shake-table testing of four full-scale URM walls in a two-way bending configuration subjected to combined out-of-plane horizontal and vertical excitation. Data Br 2020;31:105851. https://doi.org/10.1016/j.dib.2020.105851.

[29] Lourenço PB. Computations on historic masonry structures. Prog Struct Eng Mater 2002;4:301–19. https://doi.org/10.1002/pse.120.

[30] Tomaževič M. The computer program POR. Hungary: Ljubljana; 1978.

[31] Tomaževič M. Earthquake-resistant design of masonry buildings, Vol. 1. World Scientific; 1999.

[32] Magenes G, Calvi GM. In-plane seismic response of brick masonry walls. Earthq Eng Struct Dyn 1997;26:1091–112. https://doi.org/10.1002/(SICI)1096-9845(199711)26:11<1091::AID-EQE693>3.0.CO;2-6.

[33] Magenes G, Della Fontana A. Simplified non-linear seismic analysis of masonry buildings. Proc Br Mason Soc 1998;8:190–5.

[34] Chen S-Y, Moon FL, Yi T. A macroelement for the nonlinear analysis of in-plane unreinforced masonry piers. Eng Struct 2008;30:2242–52. https://doi.org/10.1016/j.engstruct.2007.12.001.

[35] Lagomarsino S, Penna A, Galasco A, Cattari S. TREMURI program: An equivalent frame model for the nonlinear seismic analysis of masonry buildings. Eng Struct 2013;56:1787–99. https://doi.org/10.1016/j.engstruct.2013.08.002.

[36] Penna A, Lagomarsino S, Galasco A. A nonlinear macroelement model for the seismic analysis of masonry buildings. Earthq Eng Struct Dyn 2014;43:159–79. https://doi.org/10.1002/eqe.2335.

[37] Addessi D, Mastrandrea A, Sacco E. A Force-Based Equivalent Frame Element for Push-Over Analysis of Masonry Structures. Key Eng Mater 2014;624:405–12. https://doi.org/10.4028/www.scientific.net/KEM.624.405.

[38] Raka E, Spacone E, Sepe V, Camata G. Advanced frame element for seismic analysis of masonry structures: model formulation and validation. Earthq Eng Struct Dyn 2015;44:2489–506. https://doi.org/10.1002/eqe.2594.

[39] Vanin F, Penna A, Beyer K. Equivalent-Frame Modeling of Two Shaking Table Tests of Masonry Buildings Accounting for Their Out-Of-Plane Response. Front. Built Environ 2020;6. https://doi.org/10.3389/fbuil.2020.00042.

[40] Vanin F, Penna A, Beyer K. A three-dimensional macroelement for modelling the in-plane and out-of-plane response of masonry walls. Earthq Eng Struct Dyn 2020. https://doi.org/10.1002/eqe.3277.

[41] Tzmatzis A, Asteris P. Finite element analysis of masonry structures: Part I-Review of previous work. 9th North Am Mason Conf 2003.

[42] Roca P, Cervera M, Gariup G, Pela' L. Structural Analysis of Masonry Historical Constructions. Classical and Advanced Approaches. Arch Comput Methods Eng 2010;17:299–325. doi:10.1007/s11831-010-9046-1.

[43] Stöckl S, Hofmann P, Mainz J. A Comparative Finite Element Evaluation of Mortar Joint Shear Tests. J Brit Mas Soc, Mason Int 1990;3:101–4.

[44] Riddington J, Fong K, Jukes P. Numerical Study of Failure Initiation in Different Joint Shear Tests. J Brit Mas Soc, Mason Int 1997;11:44–50.

[45] Gabor A, Ferrier E, Jacquelin E, Hamelin P. Analysis and modelling of the in-plane shear behaviour of hollow brick masonry panels. Constr Build Mater 2006. https://doi.org/10.1016/j.conbuildmat.2005.01.032.

[46] Adam JM, Brencich A, Hughes TG, Jefferson T. Micromodelling of eccentrically loaded brickwork: Study of masonry wallettes. Eng Struct 2010;32:1244–51. https://doi.org/10.1016/j.engstruct.2009.12.050.

[47] Kowalewski Ł, Gajewski M. Determination of failure modes in brick walls using cohesive elements approach. Procedia Eng 2015. https://doi.org/10.1016/j.proeng.2015.07.116.

[48] Andreotti G, Graziotti F, Magenes G. Detailed micro-modelling of the direct shear tests of brick masonry specimens: The role of dilatancy. Eng Struct 2018;168:929–49. https://doi.org/10.1016/j.engstruct.2018.05.019.

[49] Saw CB. Linear elastic finite element analysis of masonry walls on beams. Build Sci 1974;9:299–307. https://doi.org/10.1016/0007-3628(74)90029-2.

[50] Hendry A, Samarasinghe W, Page A. Technical Note: A finite element model for the in-plane behaviour of brickwork. Proc Inst Civ Eng 1982. https://doi.org/10.1680/iicep.1982.1878.

[51] Dhanasekar M, Kleeman P, Page A. The failure of brick masonry under biaxial stresses. Proc Inst Civ Eng 1985;79:295–313. https://doi.org/10.1680/iicep.1985.992.

[52] Lourenço PB. Computational strategies for masonry structures. PhD Thesis. Delft, The Netherlands: Delft University of Technology; 1996.

[53] Lourenço PB, Rots JG, Blaauwendraad J. Continuum Model for Masonry: Parameter Estimation and Validation. J Struct Eng 1998;124:642–52. https://doi.org/10.1061/(ASCE)0733-9445(1998)124:6(642).

[54] Berto L, Saetta A, Scotta R, Vitaliani R. An orthotropic damage model for masonry structures. Int J Numer Meth Eng 2002;55:127–57. https://doi.org/10.1002/nme.495.

[55] Lemos JV. Discrete Element Modeling of Masonry Structures. Int J Archit Herit 2007;1:190–213. https://doi.org/10.1080/15583050601176868.

[56] Mayorca P, Meguro K. Modeling Masonry Structures using the Applied Element Method. SEISAN KENKYU 2003;55:123–6.

[57] Malomo D, Pinho R, Penna A. Numerical modelling of the out-of-plane response of full-scale brick masonry prototypes subjected to incremental dynamic shake-table tests. Eng Struct 2020;209:110298. https://doi.org/10.1016/j.engstruct.2020.110298.

[58] Feyel F, Chaboche J-L. FE2 multiscale approach for modelling the elastoviscoplastic behaviour of long fibre SiC/Ti composite materials. Comput Methods Appl Mech Eng 2000;183:309–30. https://doi.org/10.1016/S0045-7825(99)00224-8.

[59] Kouznetsova V, Brekelmans WAM, Baaijens FPT. Approach to micro-macro modeling of heterogeneous materials. Comput Mech 2001;27:37–48. https://doi.org/10.1007/s004660000212.

[60] Lourenço PB, Milani G, Tralli A, Zucchini A. Analysis of masonry structures: review of and recent trends in homogenization techniquesThis article is one of a selection of papers published in this Special Issue on Masonry. Can J Civ Eng 2007;34:1443–57. doi:10.1139/L07-097.

[61] Lourenço PB, Milani G, Tralli A, Zucchini A. Analysis of masonry structures: review of and recent trends in homogenization techniques. Can J Civ Eng 2007;34:1443–57. https://doi.org/10.1139/L07-097.

[62] Milani G, Tralli A. Simple SQP approach for out-of-plane loaded homogenized brickwork panels, accounting for softening. Comput Struct 2011;89:201–15. https://doi.org/10.1016/j.compstruc.2010.09.005.

[63] Milani G, Venturini G. Automatic fragility curve evaluation of masonry churches accounting for partial collapses by means of 3D FE homogenized limit analysis. Comput Struct 2011;89:1628–48. https://doi.org/10.1016/j.compstruc.2011.04.014.

[64] Mercatoris BCN, Massart TJ. A coupled two-scale computational scheme for the failure of periodic quasi-brittle thin planar shells and its application to masonry. Int J Numer Meth Eng 2011;85:1177–206. https://doi.org/10.1002/nme.3018.

[65] Casolo S, Milani G. Simplified out-of-plane modelling of three-leaf masonry walls accounting for the material texture. Constr Build Mater 2013;40:330–51. https://doi.org/10.1016/j.conbuildmat.2012.09.090.

[66] Akhaveissy AH, Milani G. Pushover analysis of large scale unreinforced masonry structures by means of a fully 2D non-linear model. Constr Build Mater 2013;41:276–95. https://doi.org/10.1016/j.conbuildmat.2012.12.006.

[67] Lawrence S, Marshall R. Virtual Work Design Method for Masonry Panels under Lateral Load. 12th Int Brick/Block Mason Conf 2000:1063–73.

[68] AS 3700-2018:Masonry Structures, Australian Standard, Sydney, Australia 2018.

[69] Willis C. Design of unreinforced masonry walls for out-of-plane loading. University of Adelaide; 2004.

[70] Willis CR, Griffith MC, Lawrence SJ. Moment Capacities of Unreinforced Masonry Sections in Bending. Aust J Struct Eng 2006;6:133–46. https://doi.org/10.1080/13287982.2006.11464950.

[71] Griffith MC, Vaculik J. Out-of-plane flexural strength of unreinforced clay brick masonry walls. TMS J (The Mason Soc 2007.

[72] Graziotti F, Penna A, Magenes G. A comprehensive in situ and laboratory testing programme supporting seismic risk analysis of URM buildings subjected to induced earthquakes. Bull Earthq Eng 2018. https://doi.org/10.1007/s10518-018-0478-6.

[73] Leissa AW. Vibration of plates. Washington: DC, United States; 1969.

[74] RILEM TC. LUM A2 Flexural strength of masonry units, 1991. RILEM Recomm. Test. Use Constr. Mater., E & FN SPON; 1994, p. 459–61.

[75] EN 1052-5. Methods of test for masonry – Part 5: Determination of bond strength by the bond wrench method. Brussels, Belgium: European Standards, CEN/TC; 2005.

[76] EN 1052-1. Methods of test for masonry – Part 1: Determination of compressive strength. Brussels, Belgium: European Standards, CEN/TC; 1998.

[77] EN 1015-11. Methods of test for mortar for masonry – Part 11: Determination of flexural and compressive strength of hardened mortar. Brussels, Belgium: European Standards, CEN/TC; 1999.

[78] EN 1052-3. Methods of test for masonry – Part 3: Determination of initial shear strength. Brussels, Belgium: European Standards, CEN/TC; 2002.

[79] Silva LC, Lourenço PB, Milani G. Derivation of the out-of-plane behaviour of masonry through homogenization strategies: micro-scale level. Comput Struct 2018;209:30–43. https://doi.org/10.1016/j.compstruc.2018.08.013.

[80] Silva LC, Lourenço PB, Milani G. Nonlinear Discrete Homogenized Model for Out-of-Plane Loaded Masonry Walls. J Struct Eng 2017;143:4017099. https://doi.org/10.1061/(ASCE)ST.1943-541X.0001831.

[81] Anthoine A. Derivation of the in-plane elastic characteristics of masonry through homogenization theory. Int J Solids Struct 1995;32:137–63. https://doi.org/10.1016/0020-7683(94)00140-R.

[82] Geers MGD, Kouznetsova VG, Brekelmans WAM. Multi-scale computational homogenization: Trends and challenges. J Comput Appl Math 2010;234:2175–82. https://doi.org/10.1016/j.cam.2009.08.077.
[83] Otero F, Oller S, Martinez X, Salomón O. Numerical homogenization for composite materials analysis. Comparison with other micro mechanical formulations. Compos Struct 2015;122:405–16. https://doi.org/10.1016/j.compstruct.2014.11.041.
[84] Lourenço PB, Rots JG. Multisurface Interface Model for Analysis of Masonry Structures. J Eng Mech 1997;123:660–8. https://doi.org/10.1061/(ASCE)0733-9399(1997)123:7(660).
[85] Milani G, Lourenço PB, Tralli A. Homogenised limit analysis of masonry walls. Part I: Failure surfaces. Comput Struct 2006;84:166–80. https://doi.org/10.1016/j.compstruc.2005.09.005.
[86] Taliercio A. Closed-form expressions for the macroscopic in-plane elastic and creep coefficients of brick masonry. Int J Solids Struct 2014;51:2949–63. https://doi.org/10.1016/j.ijsolstr.2014.04.019.
[87] DIANA FEA. Diana User's Manual, Release 10.2. DIANA FEA BV 2017. doi: 10.1080/15421400600788682.
[88] Crisfield MA. A fast incremental/iterative solution procedure that handles "snap-through". Comput Struct 1981;13:55–62. https://doi.org/10.1016/0045-7949(81)90108-5.
[89] Love AEH. On the Small Free Vibrations and Deformations of Thin Elastic Shells. Phil Trans Roy Soc 1888.
[90] Cecchi A, Sab K. A multi-parameter homogenization study for modeling elastic masonry. Eur J Mech - A/Solids 2002;21:249–68. https://doi.org/10.1016/S0997-7538(01)01195-0.
[91] Blanco PJ, Sánchez PJ, de Souza Neto EA, Feijóo RA. Variational Foundations and Generalized Unified Theory of RVE-Based Multiscale Models. Arch Comput Methods Eng 2016;23:191–253. https://doi.org/10.1007/s11831-014-9137-5.
[92] Kawai T. New discrete models and their application to seismic response analysis of structures. Nucl Eng Des 1978;48:207–29. https://doi.org/10.1016/0029-5493(78)90217-0.
[93] Dassault Systèmes Simulia. Abaqus 6.1 2. Abaqus 612 2012.
[94] Lubliner J, Oliver J, Oller S, Oñate E. A plastic-damage model for concrete. Int J Solids Struct 1989;25:299–326. https://doi.org/10.1016/0020-7683(89)90050-4.
[95] Lee J, Fenves GL. Plastic-Damage Model for Cyclic Loading of Concrete Structures. J Eng Mech 1998;124:892–900. https://doi.org/10.1061/(ASCE)0733-9399(1998)124:8(892).
[96] Wahalathantri BL, Thambiratnam DP, Chan THT, Fawzia S. A material model for flexural crack simulation in RC using ABAQUS. Proc First Int Conf Eng Des Dev Built Environ Sustain Wellbeing 2011. https://doi.org/10.1007/BF02906653.
[97] Calvi GM, Kingsley GR, Magenes G. Testing of Masonry Structures for Seismic Assessment. Earthq Spectra 1996;12:145–62. https://doi.org/10.1193/1.1585872.
[98] Riks E. An incremental approach to the solution of snapping and buckling problems. Int J Solids Struct 1979;15:529–51. https://doi.org/10.1016/0020-7683(79)90081-7.
[99] Riks E. Some computational aspects of the stability analysis of nonlinear structures. Comput Methods Appl Mech Eng 1984;47:219–59. https://doi.org/10.1016/0045-7825(84)90078-1.
[100] Tondelli M, Beyer K, Dejong M. Influence of boundary conditions on the out-of-plane response of brick masonry walls in buildings with RC slabs. Earthq Eng Struct Dyn 2016. https://doi.org/10.1002/eqe.2710.
[101] Beyer K, Lucca F. Effect of static and kinematic boundary conditions on the out-of-plane response of brick masonry walls. Brick Block Mason. Trends, Innov. Challenges - Proc. 16th Int. Brick Block Mason. Conf. IBMAC 2016, 2016.
[102] Lawrence SJ. Behaviour of brick masonry walls under lateral loading. The University of New South Wales; 1983.
[103] Drysdale RG, Essawy AS. Out-of-Plane Bending of Concrete Block Walls. J Struct Eng 1988;114:121–33. https://doi.org/10.1061/(ASCE)0733-9445(1988)114:1(121).
[104] Vaculik J. Unreinforced masonry walls subjected to out-of-plane seismic actions. University of Adelaide; 2012.
[105] Lourenço PB. A user/programmer guide for the micro-modelling of masonry structures. 1996.
[106] AS 3700-2001:Masonry Structures, Australian Standard, Sydney, Australia 2001.
[107] Sharma S, Graziotti F, Magenes G. Torsional Shear Strength of Unreinforced Brick Masonry Bed Joints. Constr Build Mater 2020.
[108] Korswagen PA, Longo M, Rots JG. Calcium silicate against clay brick masonry: an experimental comparison of the in-plane behaviour during light damage. Bull Earthq Eng 2020;18:2759–81. https://doi.org/10.1007/s10518-020-00803-5.
[109] Silva LC, Lourenço PB, Milani G. Numerical homogenization-based seismic assessment of an English-bond masonry prototype: Structural level application. Earthq Eng Struct Dyn 2020:eqe.3267.. https://doi.org/10.1002/eqe.3267.